# A new sea ice concentration product in the polar regions derived from the FengYun-3 MWRI sensors

Ying Chen[1], Ruibo Lei[2,1], Xi Zhao[3], Shengli Wu[4,5], Yue Liu [6,1], Pei Fan[1], Qing Ji[1], Peng Zhang[4,5], Xiaoping Pang[1†]

[1]Chinese Antarctic Center of Surveying and Mapping, Wuhan University, Wuhan, 430079, China
[2]Key Laboratory for Polar Science of the MNR, Polar Research Institute of China, Shanghai, China
[3]School of Geospatial Engineering and Science, Sun Yat-Sen University & Southern Marine Science and Engineering Guangdong Laboratory, Zhuhai, China
[4]Key Laboratory of Radiometric Calibration and Validation for Environmental Satellites, National Satellite Meteorological Center (National Center for Space Weather), China Meteorological Administration, Beijing, China
[5]Innovation Center for FengYun Meteorological Satellite (FYSIC), Beijing, China
[6]Jiangsu Provincial Surveying and Mapping Engineering Institute, Nanjing, China

[†]*Correspondence to*: Xiaoping Pang (pxp@whu.edu.cn)

**Abstract.** Sea ice concentration (SIC) is the main geophysical variable for quantifying the change in sea ice in the polar regions. Continuous SIC product is very important for the studies of climate and polar marine environments. This study generates a new SIC product covering the Arctic and Antarctic from November 2010 to December 2019. It is the first long-term SIC product derived from the Microwave Radiation Imager (MWRI) sensors onboard the Chinese FengYun-3B, -3C, and -3D satellites, after a recent re-calibration of brightness temperature. We modified the previous Arctic Radiation and Turbulence Interaction Study Sea Ice (ASI) dynamic tie points algorithm mainly by changing input brightness temperature and initial tie points. The MWRI-ASI SIC was compared to the existing ASI SIC products and validated using ship-based SIC observations. Results show that the MWRI-ASI SIC mostly coincides with the ASI SIC obtained from the Special Sensor Microwave Imager series sensors, with overall biases of -1 ± 2% in the Arctic and 0.5 ± 2% in the Antarctic, respectively. The overall mean absolute deviation between the MWRI-ASI SIC and ship-based SIC is 16% and 17% in the Arctic and Antarctic, respectively, which is close to the existing ASI SIC products. The trend of sea ice extent (SIE) derived from MWRI-ASI SIC closely agrees with those of the Sea Ice Index SIEs provided by OSI-SAF and NSIDC. Therefore, the MWRI-ASI SIC is comparable with other SIC products and can be applied independently. The MWRI-ASI SIC dataset is available at https://doi.pangaea.de/10.1594/PANGAEA.945188 (Chen et al., 2022).

## 1 Introduction

The sea ice concentration (SIC) and extent (SIE), which have been continuously and regularly provided by passive microwave (PM) remote sensing for more than four decades (Trewin et al., 2021; Lavergne et al., 2022), are crucial phenological indicators for the changes in the climate and marine environment in the polar regions. The PM SIC is the most vital data to initialize the sea ice condition for climate modeling due to its continuous observations (Meier, 2019). The SIE in the polar regions has

significant annual cycles and year-to-year variations, which are closely related to the changes in climate and ecosystem in the polar regions, and global ocean circulation, suggesting significance as a climate index on both regional and global scales (Comiso et al., 2017; Parkinson and DiGirolamo, 2021; Heil et al., 2006).

Due to the long-term services of spaceborne sensors, the PM measurements can be used to continuously track the response of sea ice to climate change and support the applications for climate models or multidisciplinary studies in the polar regions. The currently operating Special Sensor Microwave Imager Sounder (SSMIS) and Advanced Microwave Scanning Radiometer 2 (AMSR2) sensors have been used for many years beyond their design lifetime (Gerland et al., 2019). The new missions for successors of these two sensors or the launch plans for other instruments, e.g., the Copernicus Imaging Microwave Radiometer (Jiménez et al., 2021) and Weather Satellite Follow–On–Microwave (Newell et al., 2020), are in the preparation stage and will be achieved in the coming years. The Chinese instruments, the Microwave Radiation Imager (MWRI) sensors onboard the FengYun-3 (FY-3) series satellites, i.e., FY-3A, FY-3B, FY-3C, and FY-3D (Zhang et al., 2018, 2019; Xian et al., 2021), are promisingly used to independently provide long-term SIC (Chen et al., 2021; Zhao et al., 2022). However, the inconsistency of different sensors and the drift of the sensor itself with increased operation time can increase the uncertainties of SIC (Eisenman et al., 2014). Thus, enriching data resources are beneficial to achieve the triple collocation between different satellites. For example, the SSMIS data has been used as a bridge to compare and connect the Advanced Microwave Scanning Radiometer-EOS (AMSR-E) and AMSR2 estimates, which have a data gap from 2011 to 2012 (Meier and Ivanoff, 2017). Besides, a new SIC product from the MWRI sensors after systematic assessment can also provide an option to verify the SIC products derived from the next generations of PM sensor.

The SIE products derived from the PM SIC products based on various sensors or algorithms revealed biases, ranging from $0.5 \times 10^6$ to $1 \times 10^6$ km$^2$, or about 3% (in winter) to 20% (in summer) of the total Arctic or Antarctic SIE (Meier and Stewart, 2019). The main factors affecting the uncertainties of SIC and SIE are the sensitivities of SIC algorithms to atmospheric emission and sea ice emissivity, especially for the thin ice or the ice in the melting stage (Ivanova et al., 2015). The SIC products with higher spatial resolutions could detect finer characteristics of the ice edge but would ignore the ice having the relatively thin thickness or melting surface, resulting in the underestimation of SIE in the marginal ice zone (MIZ) (Meier and Stewart, 2019). Thus, the uncertainties of SIC and SIE are generally greater in the melting seasons than in the freezing seasons. The uncertainties of SIC and SIE are also due to the different operations to remove spurious sea ice caused by the weather effects and land spillover (Meier and Stewart, 2019; Kern et al., 2019).

The ship-based visual observations of sea ice are the main data used for the ground validation of the satellite-based PM SIC products. To assess the performance of various algorithms for the SIC products, Spreen et al. (2008) compared the AMSR-E SICs derived from the Arctic Radiation and Turbulence Interaction Study Sea Ice (ASI), Bootstrap (BST), and enhanced NASA Team (NT2) algorithms to the ship-based SIC observations. Results indicated that the three SIC products were slightly lower than the ship-based SIC in winter but higher in summer by 10% to 12%, because the small-scale morphological features such as leads and sparse small floes are unresolved by the PM observations. Xie et al. (2013) compared the summer AMSR-E SIC to the ship-based SIC obtained in the Arctic Ocean and revealed that the AMSR-E SIC was overestimated in the Pack Ice Zone

(PIZ) but underestimated in the MIZ. Kern et al. (2019) evaluated 10 PM SIC products using the ship-based SIC observations in the polar regions with medium SIC and revealed the SIC products derived from the BST algorithm had the lowest deviations against the ship-based SIC.

70  The first generation of daily SIC dataset derived from the MWRI sensors has been released by the Chinese National Satellite Meteorological Center (NSMC) in June 2011 using the NT2 algorithm, which had a considerable positive systematic deviation compared to the SIC obtained from the Interactive Multisensor Snow and Ice Mapping System, especially at the ice edge in summer (Wu and Liu, 2018). Due to low frequencies applied in the NT2 algorithm, the original resolutions of the NT2 SIC products are lower than those of the ASI SIC products, which only uses the highest frequency with high spatial

75  resolution (Spreen et al., 2008). Zhao et al. (2022) produced a preliminary one-year Arctic SIC product derived from the FY-3D MWRI sensor using a dynamic tie points ASI algorithm, which had a smaller deviation against the AMSR2 SIC derived from the ASI algorithm compared to the products of Sea Ice Index SIC, OSI-430-b SIC, and AMSR2 SIC derived from the BST or NT2 algorithm.

In order to promote the application of MWRI sensors, this study extends the work of Zhao et al. (2022) and generates a new

80  polar SIC product from November 2010 to December 2019. The recently re-calibrated brightness temperature (TB) of the MWRI sensors provided by NSMC were used in this study to ensure the consistency of this new MWRI SIC product. The previous ASI algorithm involving dynamic tie points is modified to obtain a longer MWRI SIC product. Moreover, the MWRI-ASI SIC is compared to the existing ASI SIC products and assessed systematically using ship-based SIC observation to identify its uncertainty in various regions and seasons. We also derive SIE from the MWRI-ASI SIC and compare it to the existing SIE

85  products to test its potential for independent application.


## 2 Data and method

### 2.1 TB data from PM sensors

The MWRI sensors measure the radiation of the land, ocean, and atmosphere in conically scanning mode at five frequencies between 10 to 89 GHz at both horizontal (H) and vertical (V) polarization. The footprint size of the individual frequency ranges

90  from 9 km at 89 GHz to 85 km at 10.65 GHz. More details of the MWRI characteristics were given in Zhao et al. (2022). Although the MWRI sensors onboard the different FY-3 satellites have consistent technical characteristics, the TB data obtained from different MWRI sensors still reveal some deviations. Therefore, the MWRI TB data was re-calibrated using the operational algorithm, which focused on the hot load, antenna, and receiver calibration, reducing the TB deviations of different MWRI sensors.

95  This study used the re-calibrated level 1 swath MWRI TB data from the FY-3B, FY-3C, and FY-3D satellites, which is provided by the NSMC and available at http://www.richceos.cn (Table 1). Considering the better performance of the FY-3D MWRI sensor than others, we preferentially selected the MWRI TB from the FY-3D, followed by the FY-3C and FY-3B.

Determined by the availability and quality of the MWRI TB, the FY-3B data covered the two periods from 12 November 2010 to 30 September 2013 and from 31 May to 10 July 2015; the FY-3C lasted from 1 October 2013 to 30 May 2015 and from 11

100   July 2015 to 31 December 2017; and the FY-3D covered two years of 2018 and 2019. The re-calibrated swath MWRI TB data at 89 GHz with V- and H-polarization were applied for the ASI algorithm, and those at 18.7, 23.8, and 36.5 GHz with V-polarization were served for the weather filters. These five channels were projected onto a polar stereographic grid true at 70 degrees with a 12.5-km spatial resolution.

To evaluate the uncertainties of the re-calibrated MWRI TB in the polar regions, we chose two daily TB products, i.e., the

105   SSMI TB (version 6, Meier et al., 2021) and AMSR TB (AMSR-E version 3, Cavalieri et al., 2014; AMSR2 version 1, Meier et al., 2018), which are both available from the National Snow and Ice Data Center (NSIDC). This SSMI TB product is projected on 12.5-km and 25-km polar stereographic grids at high and low frequencies, respectively. All the frequencies of the AMSR TB products are projected on a 12.5-km polar stereographic grid. The time coverage of these two daily TB products is corresponding to that of the MWRI TB. To conduct a comparison among these three TB products, the swath MWRI TB was

110   gridded to daily MWRI TB and the low frequencies of SSMI TB were resampled to the 12.5-km polar stereographic grid. The regional TB differences were calculated in the PIZ, MIZ, and open water, respectively.

**Table 1. Summary of the datasets of TB, sea ice surface melt/freeze onset, snow depth, SIC, and SIE used in this study.**

| Parameter | Dataset | Source | Available period | Sensor | Algorithm | Resolution (km) |
|---|---|---|---|---|---|---|
| TB | MWRI TB | NSMC | 11/2010 – 12/2019 | MWRI | - | 12.5 |
| | SSMI TB | NSIDC | 11/2010 – 12/2019 | SSM/I, SSMIS | - | 25 / 12.5 |
| | AMSR TB | NSIDC | 11/2010 – 10/2011 07/2012 – 12/2019 | AMSR-E AMSR2 | - | 12.5 |
| Melt/freeze | Melt/freeze onset | GESR | 2011 – 2019 | SSM/I, SSMIS | PMA | 25 |
| Snow depth | Snow depth | NSIDC | 11/2010 – 10/2011 07/2012 – 12/2019 | AMSR-E AMSR2 | snow-depth-on-sea-ice | 12.5 |
| SIC | SSMI-ASI | Hamburg Uni. | 11/2010 – 12/2019 | SSM/I, SSMIS | ASI | 12.5 |
| | AMSR-ASI | Bremen Uni. | 11/2010 – 10/2011 07/2012 – 12/2019 | AMSR-E AMSR2 | ASI | 6.25 |
| SIE | SSMI-BST | NSIDC | 11/1978 – 12/2019 | SMMR, SSM/I, SSMIS | BST | 25 |
| | SSMI-NT | NSIDC | 11/1978 – 12/2019 | SMMR, SSM/I, SSMIS | NT | 25 |
| | Sea Ice Index | NSIDC | 11/1978 – 12/2019 | SMMR, SSM/I, SSMIS | revised NT | 25 |
| | OSI-SAF | OSI-SAF | 11/1978 – 12/2019 | SMMR, SSM/I, SSMIS | Bristol & BST | 25 |

**2.2 Existing ASI SIC products**

Two daily SIC products using the ASI algorithm in the polar regions were used as comparative data in this study (Table 1).

115   One is available from the Integrated Climate Data Center (ICDC) of the University of Hamburg, which is derived from the Special Sensor Microwave Imager series sensors projected onto a 12.5-km polar stereographic grid (SSMI-ASI) (Kern et al., 2020). The other is derived from the Advanced Microwave Scanning Radiometer series sensors projected onto a 6.25-km polar

stereographic grid (version 5.4, AMSR-ASI) produced by the Institute of Environmental Physics (IUP) of the University of Bremen (Melsheimer and Spreen, 2020). For comparison during the overlap periods with the MWRI data, we used the SSMI-ASI SIC from November 2010 to December 2019, the AMSR-E ASI SIC from November 2010 to October 2011, and the AMSR2 ASI SIC from July 2012 to December 2019, respectively. Comparisons of the daily SICs and SIEs (SIC > 15%) derived from the MWRI-ASI, SSMI-ASI, and AMSR-ASI were performed at their native spatial resolutions.

To evaluate differences in the uncertainties of SIC between the melting and freezing periods, we used the data of Arctic sea ice surface melt or freeze onset to define the ice melting and freezing periods, which (version 371s, Table 1) is available from the Goddard Earth Science Research (https://earth.gsfc.nasa.gov/index.php/cryo/data). This data is obtained from the SSMI series sensors using the passive microwave algorithm (PMA) projected onto a 25-km polar stereographic grid, which includes the onsets of the early melt, melt, freeze, and late freeze for the sea ice surface (Markus et al., 2009). We resampled the three ASI SIC products onto a 25-km grid to keep consistent with this data.

To quantify the effects of snow depth on SIC uncertainties, we obtained the snow depth on sea ice for the Arctic and Antarctic from the NSIDC (Table 1, AMSR-E version 3, Cavalieri et al., 2014; AMSR2 version 1, Meier et al., 2018). This data is derived from the AMSR TB using the AMSR-E snow-depth-on-sea-ice algorithms and projected on a 12.5-km polar stereographic grid. It is noted that this data is averaged by a five-day running window and only includes the depth of dry snow. This data provides snow depth for the entire South Ocean in the Antarctic, but only for the first-year ice in the Arctic.

To assess the observation ability of different SIC products in the MIZ, where the accuracy of PM SIC is generally low, the monthly MIZ SIE and MIZ SIE fraction (the ratio between the MIZ SIE and the total SIE) obtained from the three ASI SIC products were compared. We resampled the AMSR-ASI SIC onto a 12.5-km grid to match the MWRI-ASI SIC and SSMI-ASI SIC to compare the SIC during the entire overlap periods, as well as the winter (Arctic: December – May, Antarctic: June – November) and summer months (Arctic: June – November, Antarctic: December – May), respectively. To evaluate the uncertainties of SIC under different SIC scenarios, we divided SIC into three levels: low SIC (15–30%), medium SIC (30–70%), and high SIC (70–100%), and calculated the SIC differences among the ASI SIC products within each SIC categorization.

**2.3 Existing monthly SIE products**

This study used four products of monthly SIE in the polar regions from November 1978 to December 2019 (Table 1), which are all derived from SIC products at a 25-km grid resolution obtained from the SSMI series sensors. The NSIDC provides the SIE products using the BST and NASA Team algorithms (SSMI-BST and SSMI-NT) (Stroeve and Meier, 2018), as well as the SIE product derived from the Sea Ice Index SIC product (version 3) (Fetterer et al., 2017). The fourth SIE product is derived from the SIC product developed by the Ocean and Sea Ice Satellite Application Facility Norwegian Meteorological Institute (version 2, OSI-SAF) (Lavergne et al., 2020).

The differences between the MWRI-ASI SIE and four existing SIE products were quantified during their entire overlap periods, as well as the winter and summer months. The 2010–2019 trends of the MWRI-ASI SIE and four existing SIE products were

compared. Moreover, to test the capability of the MWRI-ASI SIE as an independent data for climate studies, we performed an analysis of combined SIE trends. The 40-year (1979 to 2019) trends combining the four existing SIE products from January 1979 to November 2010 and MWRI-ASI SIE from December 2010 to December 2019 were compared to the original trends derived from the four existing SIE products.

## 2.4 Modified ASI dynamic tie points algorithm

In the previous study (Zhao et al., 2022), a TB bias-correction was performed to reduce the biases between daily MWRI TB and AMSR2 TB. An ASI algorithm involving daily dynamic tie points was applied in the Arctic. The tie points of AMSR series were used as the initial tie points, and the daily dynamic tie points were generated according to the initial SIC, locations, and time sliding window. Two weather filters and a monthly maximum ice extent mask were utilized to remove the spurious sea ice. More details about the dynamic tie points ASI algorithm were given in Zhao et al. (2022), and the details about the ASI algorithm can be referred to Svendsen et al., (1987), Kaleschke et al. (2001) and Spreen et al. (2008).

To obtain a longer dataset of MWRI SIC and optimize the estimation procedures, this study modified the previous algorithm from the five aspects (Table 2). The detailed procedures for retrieving this MWRI-ASI SIC product can be seen in the supplement file. Using daily TB would dilute the atmospheric signal due to the nonlinear atmospheric influence on the TB (Comiso et al., 2003). Thus, this study used the re-calibrated swath MWRI TB to calculate SIC and gridded the swath SIC into daily SIC.

**Table 2. Differences in the parameters or operations used in the previous and modified algorithms.**

| Parameter/operation | Previous algorithm | Modified algorithm |
|---|---|---|
| input TB | daily MWRI TB bias-corrected to daily AMSR2 TB | swath re-calibrated MWRI TB |
| swath into daily | swath TB into daily TB | swath SIC into daily SIC |
| initial tie points | $P_I$ =11.7 K, $P_0$ = 47 K (Arctic) | $P_I$ =7.1 K, $P_0$ = 50.3 K (Arctic)<br>$P_I$ =7.3 K, $P_0$ = 55.9 K (Antarctic) |
| dynamic tie points (Antarctic) | - | $P_I$: initial SIC larger than 95% within the monthly minimum ice extent, 100 km away from the coast.<br>$P_0$: initial SIC within [-10%, 10%], between 200 and 350 km away from the monthly ice edge, 100 km away from the coast. |
| weather filters | GR(36.5/18.7): 0.045; GR(23.8/18.7): 0.04 | GR(36.5/18.7): 0.05; GR(23.8/18.7): 0.045 |

Zhao et al. (2022) directly used the tie points of AMSR series as initial tie points, which would cause large uncertainties in initial SIC due to differences between MWRI and AMSR TB. Thus, this study proposed a new operation to generate the initial tie points. We tested the sea ice tie points ($P_I$) from 6.0 to 12.0 K and the open water tie points ($P_0$) from 47.0 to 57.0 K with an interval of 0.1 K. Based on these 6000 pairs of tie points, the swath MWRI SIC was calculated from the swath TB using the ASI algorithm and then averaged into daily SIC. We used daily SSMI-ASI SIC in 2018 as the referential SIC and computed

the daily average of the MWRI-ASI SIC and SSMI-ASI SIC (SIC > 15%). Then, the linear regression was conducted between the daily average MWRI-ASI SIC and referential SSMI-ASI SIC. We selected one pair of tie points as initial tie points by satisfying requirements with the slope closer to 1, intercept closer to 0, and relatively low standard deviation (Std) among the 6000 samples. According to the above procedures, the initial $P_1$ were defined as 7.1 and 7.3 K, and the $P_0$ were determined as 50.3 and 55.9 K in the Arctic and Antarctic, respectively. This parameterization of $P_1$ and $P_0$ can effectively reduce the differences between the initial MWRI SIC and referential SSMI SIC. The steps for generating the initial points are given in more details in Section S1.2 of the supplement file.

As the Arctic dynamic tie points proposed in Zhao et al. (2022), this study also generated the Antarctic dynamic tie points. The conditions of sea ice tie-point samples are defined as follows: the initial SICs of grids are larger than 95%, and the grids are within the monthly minimum ice extent and 100 km away from the coast. The conditions of open water tie-point samples are defined as follows: the initial SICs of grids fall within the range [-10%, 10%], and the grids are away from the monthly ice edge by 200–350 km and away from the coast by 100 km. The Section S1.4 of the supplement file illustrates detailed procedures of generating the dynamic tie points.

The thresholds of the weather filters GR(36.5/18.7) and GR(23.8/18.7) were determined as 0.045 and 0.04 by Zhao et al. (2022), respectively, as the AMSR series sensors. In this study, we chose 0.05 and 0.045 as thresholds of GR(36.5/18.7) and GR(23.8/18.7), respectively, as the SSMI series sensors, which can generally remove the weather effects (Gloersen and Cavalieri, 1986; Cavalieri et al., 1995). Here, the GR is defined as the TB difference with V-polarization between high and low frequencies against to the sum of these two TB.

**2.5 Ship-based observation data**

The ship-based observations of sea ice follow the protocols of the Ice Watch/Arctic Ship-based Sea-Ice Standardization (Ice Watch/ASSIST) (Hutchings et al., 2019) in the Arctic and of the Antarctic Sea Ice Processes and Climate (ASPeCt) (Worby and Allison, 1999) in the Antarctic. The two protocols have the same observation principle for SIC, and their main difference is the description of the surface properties of sea ice, such as the quantitative description of the melt pond coverage for Arctic sea ice by the Ice Watch/ASSIST. To validate the accuracy of the MWRI-ASI SIC, we collected the observational SIC from various ship-based measurement programs of the Chinese National Arctic and Antarctic Research Expedition (CHINARE) conducted by the Polar Research Institute of China (Lei et al., 2017) and a standardized ship-based observation dataset (ESA-SICCI) produced by Kern (2019), as well as those available in the IceWatch (https://icewatch.met.no/cruises) and PANGAEA databases (https://www.pangaea.de).

A total of 8887 and 3882 samples of ship-based observations in the Arctic and Antarctic, respectively, obtained from December 2010 to November 2019 were used here. Among them, 10726 and 2043 samples were obtained from the summer and winter months, respectively. We projected the ship-based SIC onto the polar stereographic grid and computed the average of the ship-based samples obtained in one calendar day within one polar stereographic grid corresponding to the PM SIC sample. A total of 5230, 5508, and 6169 samples of the ship-based SIC corresponding to the MWRI-ASI, SSMI-ASI, and AMSR-ASI products

were used in the Arctic, respectively, about 88% (12%) of which were obtained from the summer (winter) months. In the Antarctic, we collected 2599, 2613, and 2979 ship-based SIC samples corresponding to the MWRI-ASI, SSMI-ASI, and AMSR-ASI products, respectively, about 73% (27%) of which were obtained from the summer (winter) months.

210 We compared the three ASI SIC products to the ship-based SIC by calculating the bias, mean absolute deviation (MAD), root mean standard deviation (RMSD), and correlation coefficient ($R$) during the entire overlap periods, as well as the summer and winter months separately, at their native spatial resolutions. To evaluate the impact of sea ice conditions on the accuracy of SIC, we divided SIC as low (15–30%), medium (30–70%), and high (70–100%) levels.
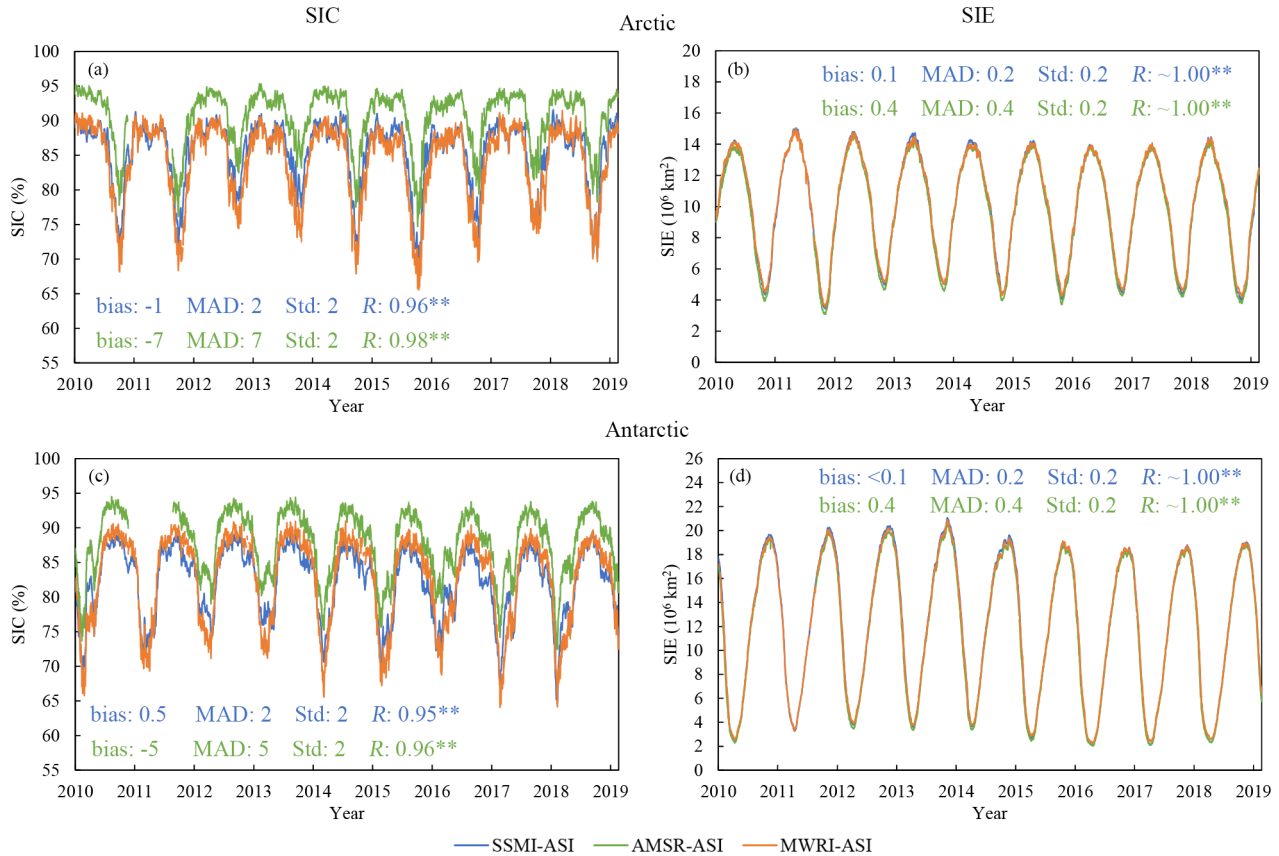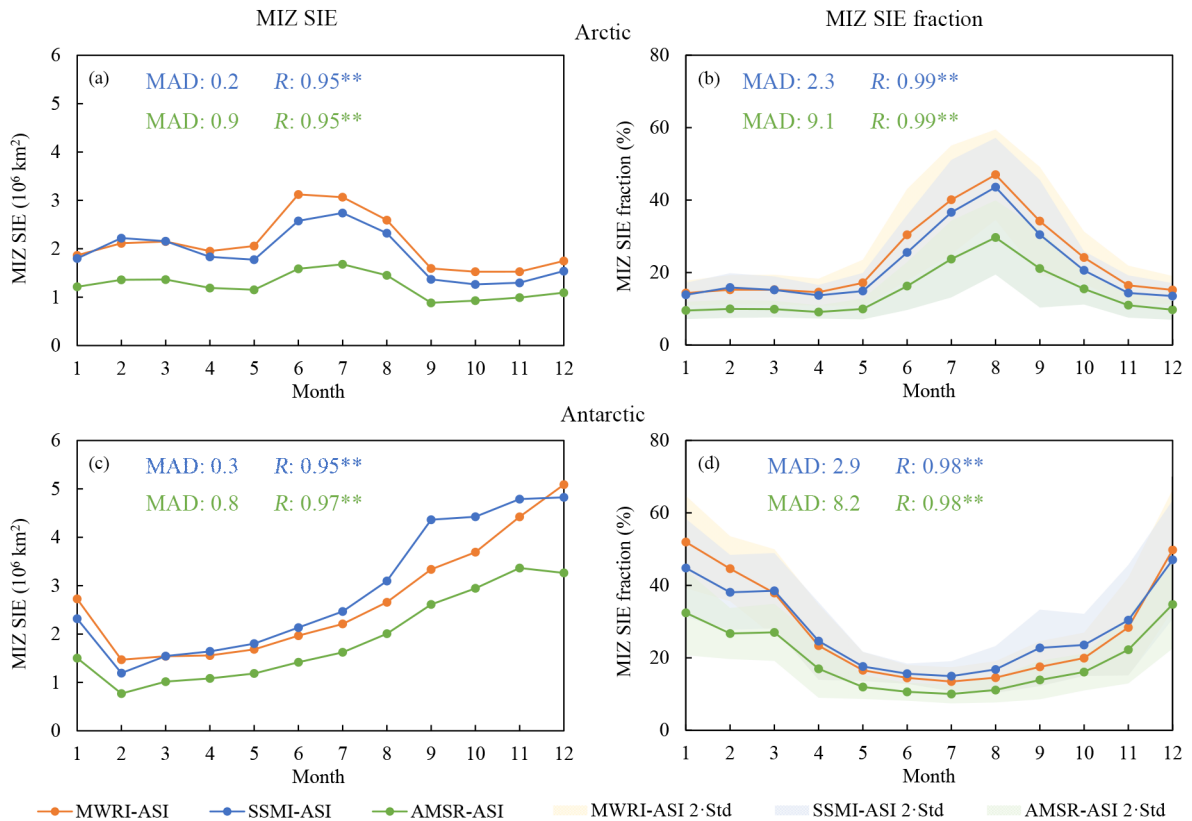


215 **Figure 1: Daily average SIC and daily SIE from November 2010 to December 2019. Also shown are the differences in SIC and SIE between the MWRI-ASI and SSMI-ASI (blue number) and between the MWRI-ASI and AMSR-ASI (green number). The statistically significant at 95% and 99% confidence levels are marked by * and **, respectively, and those below 95% confidence level are not marked, the same below.**

8

## 3 Results

### 3.1 Comparisons of the ASI SIC products

All the three ASI SIC products reveal similar variation patterns in daily SIC and SIE (Fig. 1), with $R$s between each pair of products larger than 0.95 ($P<0.01$). The MWRI-ASI SIC is much closer to the SSMI-ASI SIC with overall biases of -1% and 0.5% in the Arctic and Antarctic, respectively, compared to the AMSR-ASI SIC. Both the MWRI-ASI SIC and SSMI-ASI SIC are lower than the AMSR-ASI SIC by about 5% in the bipolar regions. The MADs of SIE between the MWRI-ASI and SSMI-ASI are lower than those between the MWRI-ASI and AMSR-ASI by $0.2\times10^6$ km$^2$ (or 2% of the mean total SIE) in the bipolar regions. Compared to the AMSR-ASI, the relatively small differences in SIC and SIE of the MWRI-ASI against the SSMI-ASI is likely because the initial tie points computation of the MWRI-ASI SIC was referred to the SSMI-ASI SIC.



**Figure 2:Monthly MIZ SIE and MIZ SIE fraction from November 2010 to December 2019. Also shown are the differences in MIZ SIE and MIZ SIE fraction between the MWRI-ASI and SSMI-ASI (blue number) and between the MWRI-ASI and AMSR-ASI (green number). The shades present the 2 Stds from the monthly MIZ SIE fraction.**

Compared to the total SIE, the MADs of MIZ SIE between the MWRI-ASI and SSMI-ASI increase by $0.04\times10^6$ and $0.1\times10^6$ km$^2$, and those between the MWRI-ASI and AMSR-ASI increase by $0.5\times10^6$ and $0.4\times10^6$ km$^2$ in the Arctic and Antarctic, respectively (Fig. 2). It suggests that the deviations of different SIC products increase significantly in the MIZ compared to

235    the total ice region. Seasonally, the MWRI-ASI MIZ SIE reveals the smallest deviation against the SSMI-ASI MIZ SIE in March for the bipolar regions. However, the influence regime is different between the Arctic and Antarctic. In the Arctic, fewer spurious ice along the coast caused by land spillover is introduced into the MIZ SIE estimation in March, when the SIE reaches the maximum, reducing the deviation between two SIEs. In the Antarctic, lower MWRI-ASI MIZ SIE is exactly compensated by the spurious ice caused by land spillover and weather effects in March, leading to a near-zero bias between two SIEs.

240    two SIEs. In the bipolar regions, the differences in MIZ SIE between the MWRI-ASI and AMSR-ASI are lower in winter than in summer when the MIZ SIE fraction is higher. The MIZ SIEs obtained from the MWRI-ASI SIC and SSMI-ASI SIC are larger than that obtained from the AMSR-ASI SIC, because lower grid resolutions of the MWRI-ASI and SSMI-ASI lead to smearing at the ice edge and overestimation of MIZ SIE. Moreover, the MIZ SIE fraction of the AMSR-ASI is lower than those of the MWRI-ASI and SSMI-ASI, because the total AMSR-ASI SIC is relatively high (Fig. 1) and more grids at the

245    boundary between the MIZ and PIZ have been identified as the PIZ by the AMSR-ASI compared to the MWRI-ASI and SSMI-ASI.

   Spatially, the MWRI-ASI SIC is slightly smaller than the SSMI-ASI SIC in the PIZ in the Arctic, while larger along the coastline and ice edge (Fig. 3), as the MWRI-ASI has more residual ice caused by land spillover and weather effects compared to the SSMI-ASI. In the Antarctic, the MWRI-ASI SIC is generally higher than the SSMI-ASI SIC. Compared to the AMSR-

250    ASI SIC, the MWRI-ASI SIC is underestimated in the pan Arctic Ocean and in the PIZ in the Antarctic, while overestimated at the ice edge in the Antarctic. Note that the apparent stripes of SIC differences between the MWRI-ASI and SSMI-ASI are located at the low latitude regions in the bipolar regions (Fig. 3a, 3b, 3g, and 3h), which are due to the raw stripes of the SSMI-ASI SIC.

   In the Arctic and Antarctic, the lowest SIC differences both appear in the region with high SIC (70–100%) (Fig. 4), with mean

255    MAD of 4% between the MWRI-ASI and SSMI-ASI and of 5% between the MWRI-ASI and AMSR-ASI, respectively. The largest MAD (16%) between the MWRI-ASI SIC and SSMI-ASI SIC is identified in the region with low SIC (15–30%), and the MAD between the MWRI-ASI SIC and AMSR-ASI SIC is the highest (16%) in the region with medium SIC (30–70%) or low SIC (15–30%). Thus, the differences among the ASI SIC products are smaller in the regions of high SIC than in the regions with low or medium SIC.

260    In the Arctic, in the freezing period of sea ice surface from late freeze onset to early melt onset, the SIC differences are lower with MAD of 3% between the MWRI-ASI and SSMI-ASI and of 4% between the MWRI-ASI and AMSR-ASI, respectively, compared to those (6% and 9%) in the surface melting period from melt onset to freeze onset. The MWRI-ASI SIC is higher than the SSMI-ASI SIC in the surface freezing stage but slightly smaller in the surface melting stage. These indicate that the differences among the ASI SIC products are larger in the surface melting state than in the surface freezing state and that the

265    MWRI-ASI is more sensitive to melting ice surface than the SSMI-ASI.
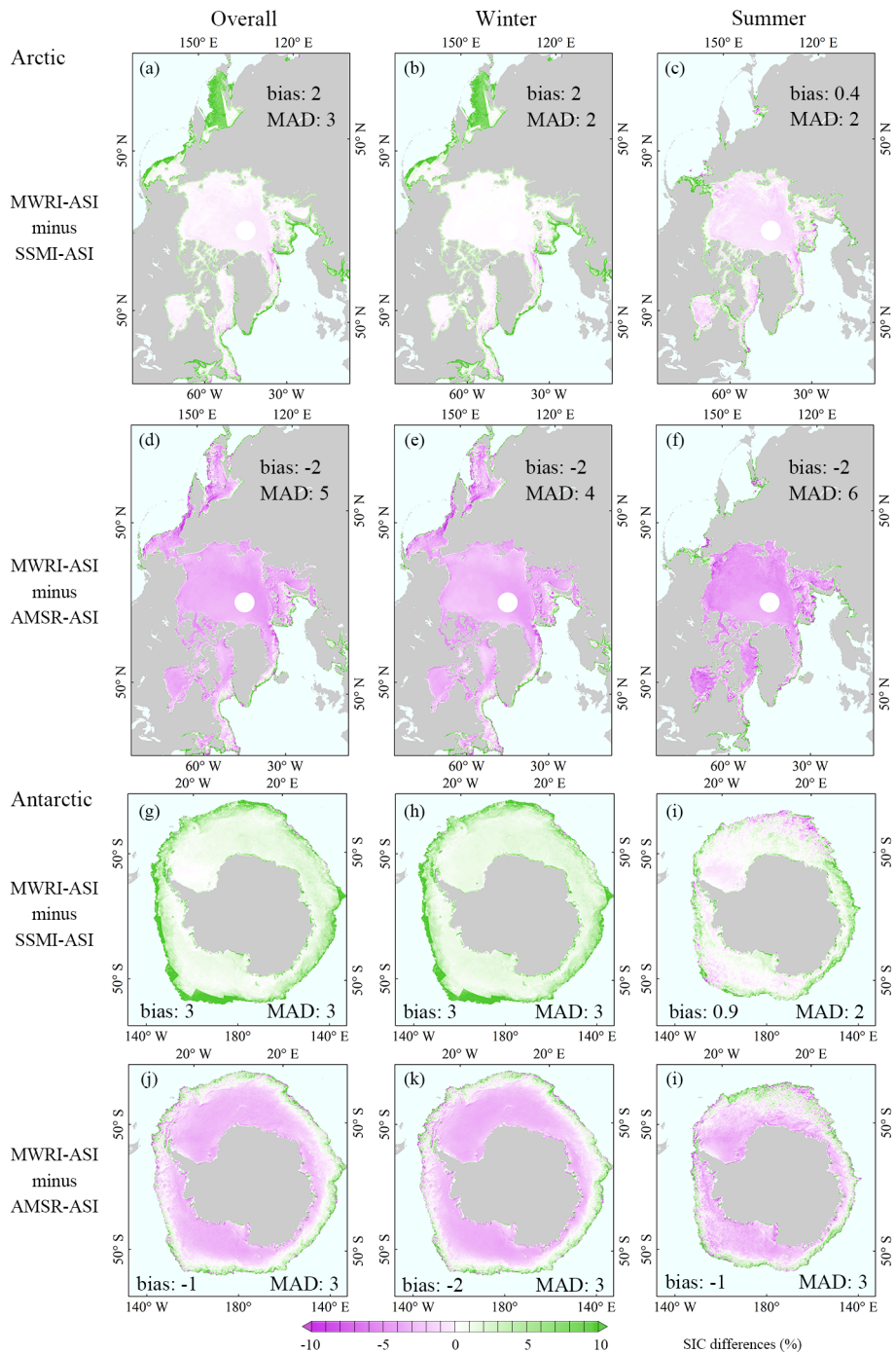
**Figure 3: SIC differences between the MWRI-ASI and SSMI-ASI and between the MWRI-ASI and AMSR-ASI during the entire overlap periods, as well as the winter and the summer months from November 2010 to December 2019. The grey is land, and the cyan is open water.**
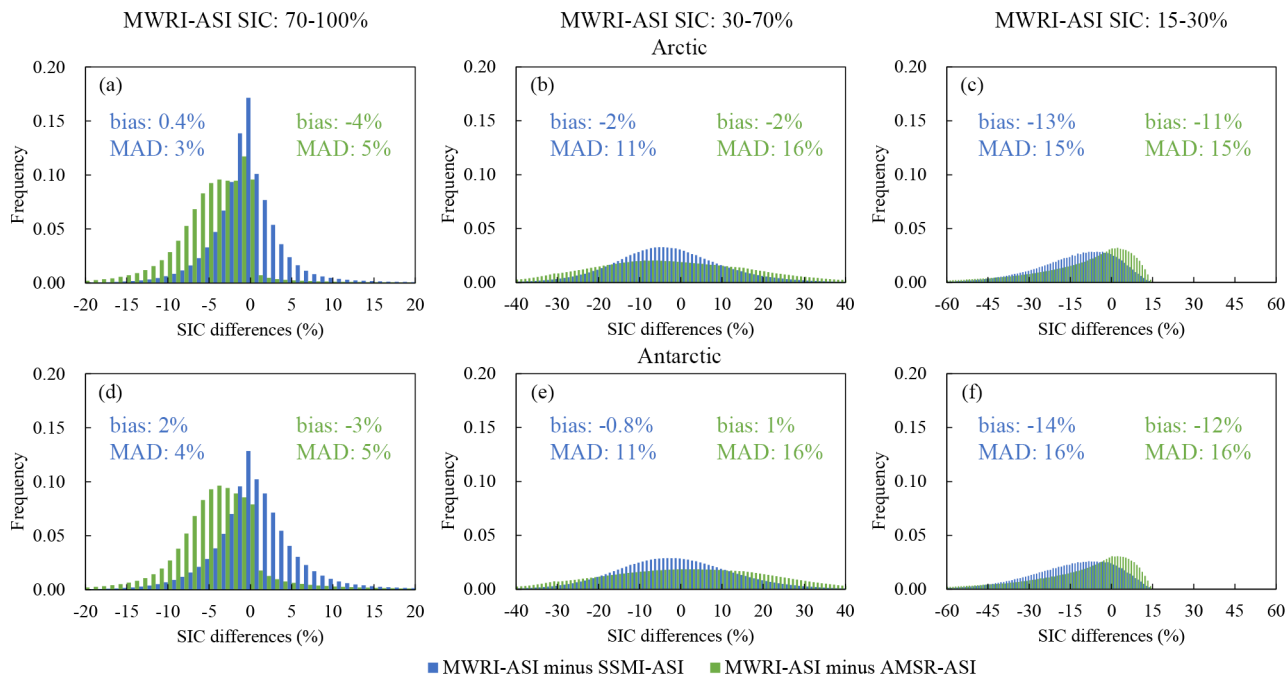
**Figure 4: Histogram of SIC differences between the MWRI-ASI and SSMI-ASI and between the MWRI-ASI and AMSR-ASI with the MWRI-ASI SIC of 70–100%, 30–70%, and 15–30% from November 2010 to December 2019. Also shown are the differences in SIC between the MWRI-ASI and SSMI-ASI (blue number) and between the MWRI-ASI and AMSR-ASI (green number).**
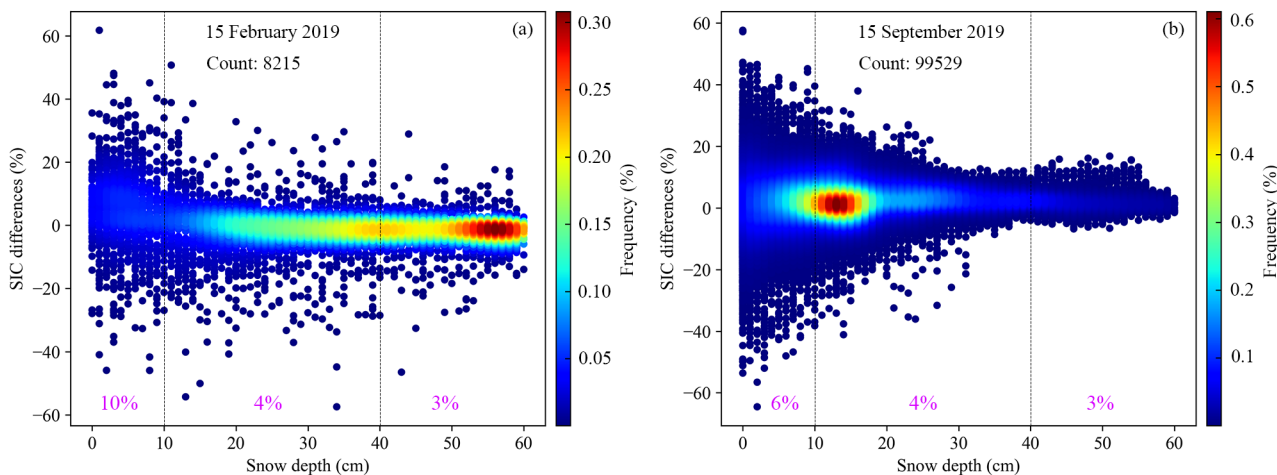


**Figure 5: Frequency of SIC differences between the MWRI-ASI and SSMI-ASI with different snow depths in the Antarctic on 15 February (a) and 15 September (b) 2019. The purple numbers present the MADs in SIC between the MWRI-ASI and SSMI-ASI with the snow depth of 0-10 cm, 10-40 cm, and 40-60 cm.**

When the snow depth is lower than 10 cm, the SIC differences are the largest with a mean MAD of 7% between the MWRI-ASI and SSMI-ASI and of 9% between the MWRI-ASI and AMSR-ASI, which are about three times of those (2% and 3%)

when the snow depth is higher than 40 cm (Table S2 of the supplement file). One of the reasons is that the TB differences are also largest when the snow depth is lower than 10 cm, about twice as much as when the snow depth is higher than 10 cm (Table S3 of the supplement file). The spatial distribution of SIC differences do not show the obvious variability with the snow depth (Fig. 3), because all the SIC products are retrieved by the ASI algorithm, which have the consistent sensitivity to snow depth. In the Antarctic (Fig. 5), when the snow depth is lower than 10 cm, the MAD between MWRI-ASI SIC and SSMI-ASI SIC is 10% on the example day in summer, which are larger than those in winter by 4%. This could be explained by metamorphoses in the properties of snow over sea ice during summer, such as increased wetness (even saturated with meltwater), increased snow density, increased snow grain size, the occurrence of diurnal melt–refreeze cycles on surface, and slush on surface, etc., which have an impact on TB (Ivanova et al., 2015; Kern et al., 2016, 2019). The increase of snow wetness usually leads to an increase in TB of about 10 - 60 K, while the increase of snow grain size, which would cause the geophysical properties of snow cover to be very close to the surface scattering layer of sea ice, typically leads to a decrease in TB of about 15 - 35 K, resulting in large uncertainty of SIC (Kern et al., 2016). With the increase in snow depth, e.g., > 40 cm, the corresponding increased snow load may lead to a negative ice freeboard, especially for the thin ice in the Antarctic, resulting in the slush layer appearing between the snow cover and the ice layer (Li et al., 2023). However, such slush layer is often thin, and the surface covered with thick snow would generally keep dry. This mechanism can be used to explain why the deviation of SIC is always the smallest for thick snow cover in both winter or summer. Thus, the snow over sea ice could play a significant role on the SIC uncertainties, which is greater at lower snow depth, especially in summer.

## 3.2 Comparisons of the SIE products

In the Arctic, the MWRI-ASI SIE is smaller than the four existing SIE products of SSMI-NT, SSMI-BST, OSI-SAF, and Sea Ice Index, and has the smallest difference against the Sea Ice Index SIE with an overall MAD of $0.3 \times 10^6$ km$^2$ (Table 3). In the Antarctic, the MWRI-ASI SIE is larger than the Sea Ice Index SIE and lower than the other three SIE products, and it has the smallest differences against the Sea Ice Index SIE and OSI-SAF SIE, with an overall MAD of $0.2 \times 10^6$ km$^2$.

**Table 3. Biases and MADs between the MWRI-ASI SIE and the four existing SIE products during the entire overlap periods, as well as the winter and summer months from December 2010 to December 2019. The underlined numbers represent the lowest biases and MADs.**

| | | Overall ($10^6$ km$^2$) | | Winter ($10^6$ km$^2$) | | Summer ($10^6$ km$^2$) | |
|---|---|---|---|---|---|---|---|
| | | bias | MAD | bias | MAD | bias | MAD |
| Arctic | SSMI-BST | -0.9 | 0.9 | -0.9 | 0.9 | -0.9 | 0.9 |
| | SSMI-NT | -0.6 | 0.6 | -0.7 | 0.7 | -0.5 | 0.5 |
| | OSI-SAF | -0.7 | 0.7 | -0.7 | 0.7 | -0.7 | 0.7 |
| | Sea Ice Index | <u>-0.3</u> | <u>0.3</u> | <u>-0.5</u> | <u>0.5</u> | <u>-0.2</u> | <u>0.2</u> |
| Antarctic | SSMI-BST | -0.5 | 0.5 | -0.3 | 0.3 | -0.6 | 0.6 |
| | SSMI-NT | -0.2 | 0.3 | <0.1 | 0.2 | -0.4 | 0.4 |
| | OSI-SAF | <u>-0.2</u> | <u>0.2</u> | <u>-0.1</u> | <u>0.1</u> | -0.3 | 0.3 |
| | Sea Ice Index | <u>0.2</u> | <u>0.2</u> | 0.4 | 0.4 | <u>0.1</u> | <u>0.1</u> |

From 2010 to 2019, the MWRI-ASI SIE shows a significant decline trend of -49,214 km$^2$ yr$^{-1}$ ($P<0.01$) in the Arctic and has the smallest difference in trends (-509 km$^2$ yr$^{-1}$ or about 1%) against the SSMI-NT SIE (Table 4). In the Antarctic, the largest decreasing trend is identified for the MWRI-ASI SIE (-191,993 km$^2$ yr$^{-1}$, $P<0.01$), and the difference in trends between the MWRI-ASI SIE and OSI-SAF SIE is the lowest (-8,928 km$^2$ yr$^{-1}$ or about 5%).

310     In the period from 1979 to 2019, the four existing SIE products show significant decreasing trends (about -55,000 km$^2$ yr$^{-1}$, $P<0.01$) in the Arctic and increasing trends (about 7,500 km$^2$ yr$^{-1}$, $P<0.01$) in the Antarctic (Table 4). The decreasing trends ($P<0.01$) of the combined SIEs in the Arctic are larger (by 15% to 40%) than those of the original SIEs because the MWRI-ASI SIE is lower than the four existing SIEs from 2010 to 2019. For the combination of the Sea Ice Index SIE and MWRI-ASI SIE in the Arctic, the differences in trends between the original and combined SIEs are the smallest (-8,343 km$^2$ yr$^{-1}$ or about 15%) compared to other combinations. In the Antarctic, the relatively small increasing trend of the original SSMI-BST SIE is reversed by the SIE combination of the SSMI-BST and MWRI-ASI due to lower MWRI-ASI SIE. The trend combining the Sea Ice Index SIE and MWRI-ASI SIE ($P<0.01$) in the Antarctic is larger than the original Sea Ice Index SIE trend because the MWRI-ASI SIE is higher than the Sea Ice Index SIE from 2010 to 2019. The combined Antarctic SIE trend of the OSI-SAF and MWRI-ASI ($P<0.05$) has the lowest differences (-4,736 km$^2$ yr$^{-1}$ or about 50%) against the original OSI-SAF SIE trend, compared to other combined SIE trends. Seasonally, in the Arctic, the differences in trends between the original and combined SIEs are larger in winter than in summer, because the differences between the MWRI-ASI SIE and four existing SIEs are larger in winter than in summer when more coastal sea ice are identified by the MWRI-ASI reducing the absolute deviations. In the Antarctic, the summer trends of the original SIEs are insignificant, but the significant winter increasing trends ($P<0.05$) are identified by all original SIEs and combined SIEs, except for the combination of the SSMI-BST SIE and MWRI-ASI SIE. Thereby, using the MWRI-ASI SIE instead of the original SIEs to construct a new time series has a greater impact on identifying the changing trend in SIE of the Antarctic than that of the Arctic because the Antarctic SIE trend is not as obvious as that of the Arctic.

    For the Arctic annual maximum SIEs from 2011 to 2019, the ranking provided by the MWRI-ASI is the same as those provided by the SSMI-BST and Sea Ice Index, and all the largest values were observed in March 2012 for the five SIEs (Fig. 6). For the Arctic annual minimum SIEs, all the five SIEs identify the smallest and second-smallest values in September 2012 and 2019, respectively. The five SIEs have different rankings for 2013 and 2014 when the two largest Arctic annual minimum SIEs in 2011–2019 appeared, and the MWRI-ASI identifies the largest value in 2013, as the SSMI-BST and SSMI-NT. The five SIEs provide the same ranking of the Antarctic annual maximum SIEs and identify the largest and smallest SIEs in September 2014 and 2017, respectively, indicating the sudden drop after 2014 and rise after 2017 of Antarctic SIE can be depicted by all the five SIEs. The MWRI-ASI SIE reveals the smallest Antarctic annual minimum SIEs in 2017, as the SSMI-BST, OSI-SAF, and Sea Ice Index, but the SSMI-NT identifies the smallest value ($2.4 \times 10^6$ km$^2$) in 2018, which is slightly smaller than those in 2017 by $0.005 \times 10^6$ km$^2$. The MWRI-ASI has the same ranking for the five largest Antarctic annual minimum SIEs as the SSMI-BST and SSMI-NT. Thereby, the MWRI-ASI SIE is reasonable for identifying the extreme cases of both the annual

maximum and minimum SIEs in the bipolar regions, only with small differences appearing in some individual years with

340 relatively low year-to-year differences.

**Table 4. Trends of the MWRI-ASI SIE and the four existing SIE products, and differences in trends between the MWRI-ASI SIE and the four existing SIE products from December 2010 to December 2019. Original trends of the four existing SIE products, combined trends (January 1979 to November 2010: four existing SIE products; December 2010 to December 2019: MWRI-ASI), and differences in trends between the original and combined SIEs from January 1979 to December 2019. The underlined numbers**

345 **represent the lowest differences.**

| | | 2010 – 2019 (km² yr⁻¹) | | 1979 – 2019 (km² yr⁻¹) | | |
|---|---|---|---|---|---|---|
| | | Trend | Differences | Original trend | Combined trend | Differences |
| Arctic | MWRI-ASI | -49,214 ± 10,884** | - | - | - | - |
| | SSMI-BST | -58,279 ± 12,654** | 9,065 | -57,644 ± 1,511** | -80,653 ± 1,831** | -23,009 |
| | SSMI-NT | -48,705 ± 12,672** | <u>-509</u> | -55,879 ± 1,504** | -70,205 ± 1,608** | -14,326 |
| | OSI-SAF | -50,705 ± 11,529** | 1,491 | -53,379 ± 1,395** | -70,653 ± 1,567** | -17,274 |
| | Sea Ice Index | -45,527 ± 12,229** | -3,687 | -56,330 ± 1,489** | -64,673 ± 1,440** | <u>-8,343</u> |
| Antarctic | MWRI-ASI | -191,993 ± 25,790** | - | - | - | - |
| | SSMI-BST | -181,269 ± 25,942** | -10,724 | 6,057 ± 2,192** | -5,834 ± 2,400* | -11,891 |
| | SSMI-NT | -178,209 ± 26,145** | -13,784 | 6,995 ± 2,189** | 1,628 ± 2,305 | -5,367 |
| | OSI-SAF | -183,065 ± 25,547** | <u>-8,928</u> | 9,567 ± 2,171** | 4,831 ± 2,253* | <u>-4,736</u> |
| | Sea Ice Index | -176,685 ± 25,461** | -15,308 | 7,436 ± 2,138** | 13,433 ± 2,192** | 5,997 |
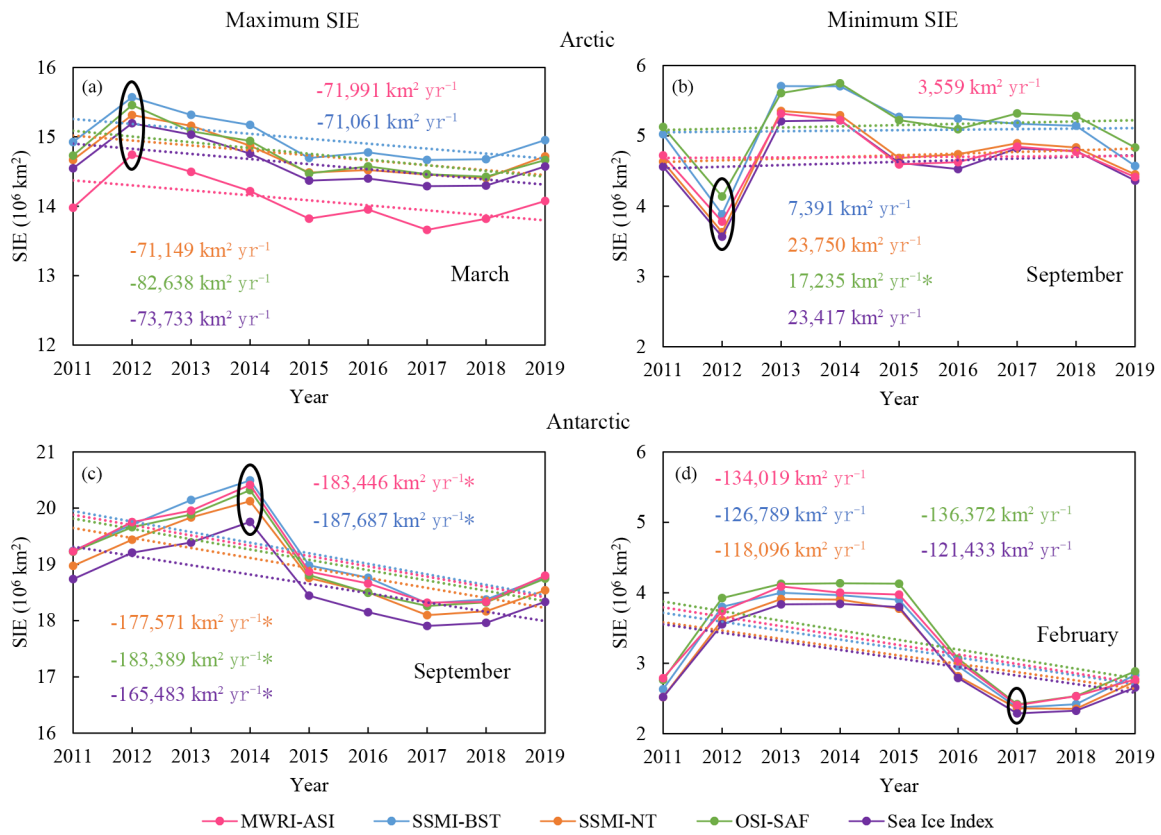
**Figure 6: Annual maximum and minimum SIEs from 2011 to 2019. Also shown are the corresponding SIE trends of the MWRI-ASI (pink), SSMI-BST (blue), SSMI-NT (orange), OSI-SAF (green), and Sea Ice Index (purple). The black circles present the largest annual maximum or the smallest annual minimum SIE. Note that the smallest Antarctic annual minimum SIE of the SSMI-NT is observed in February 2018.**
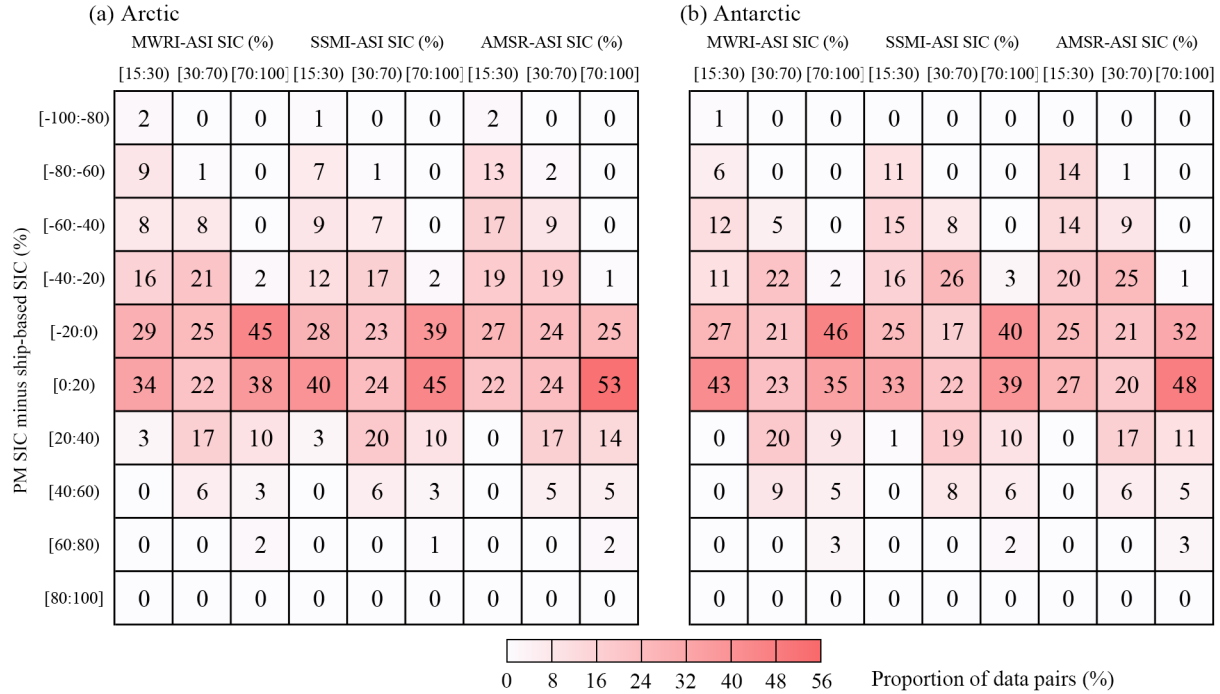
### 3.3 Comparisons to the ship-based SIC

The differences between the MWRI-ASI SIC and ship-based SIC are concentrated from -20% to 20%, generally accounting for 71% and 68% of the total samples in the Arctic and Antarctic, respectively (Fig. 7). In the region with high SIC (70–100%), about 82% of SIC differences between the MWRI-ASI and ship-based observation are distributed from -20% and 20%. However, this value decreases to about 67% and 46% in the regions with low SIC (15–30%) and medium SIC (30–70%), respectively. The MWRI-ASI SIC has smaller differences against the ship-based SIC in the regions with SIC above 70%, with MADs of 12% in both the Arctic and Antarctic, compared to those (16% and 17%) obtained for all samples.

Seasonally, in summer, the MADs between the MWRI-ASI SIC and ship-based SIC are 17% in the Arctic and 18% in the Antarctic, respectively, increasing by 5% compared to those in winter (Table 5). This implies that the MWRI-ASI SIC has a better accuracy in winter than in summer, which is due to the high sensitivity of PM signal to atmospheric and ice surface melting conditions.

16

Spatially (Fig. 8), the SIC differences between the MWRI-ASI and ship-based observations within 50 km away from the coast are larger with MAD of 23% in the Arctic and of 22% in the Antarctic, respectively, compared to those (16%) beyond 50 km away from the coast. It illustrates that, compared to the ship-based observations, the MWRI-ASI SIC has comparable accuracy with the SSMI-ASI SIC and AMSR-ASI SIC, although the accuracy of the MWRI-ASI SIC can be affected by the coast to a slight degree.

(a) Arctic

PM SIC minus ship-based SIC (%)

| | MWRI-ASI SIC (%) | | | SSMI-ASI SIC (%) | | | AMSR-ASI SIC (%) | | |
|---|---|---|---|---|---|---|---|---|---|
| | [15:30) | [30:70) | [70:100] | [15:30) | [30:70) | [70:100] | [15:30) | [30:70) | [70:100] |
| [-100:-80) | 2 | 0 | 0 | 1 | 0 | 0 | 2 | 0 | 0 |
| [-80:-60) | 9 | 1 | 0 | 7 | 1 | 0 | 13 | 2 | 0 |
| [-60:-40) | 8 | 8 | 0 | 9 | 7 | 0 | 17 | 9 | 0 |
| [-40:-20) | 16 | 21 | 2 | 12 | 17 | 2 | 19 | 19 | 1 |
| [-20:0) | 29 | 25 | 45 | 28 | 23 | 39 | 27 | 24 | 25 |
| [0:20) | 34 | 22 | 38 | 40 | 24 | 45 | 22 | 24 | 53 |
| [20:40) | 3 | 17 | 10 | 3 | 20 | 10 | 0 | 17 | 14 |
| [40:60) | 0 | 6 | 3 | 0 | 6 | 3 | 0 | 5 | 5 |
| [60:80) | 0 | 0 | 2 | 0 | 0 | 1 | 0 | 0 | 2 |
| [80:100] | 0 | 0 | 0 | 0 | 0 | 0 | 0 | 0 | 0 |

(b) Antarctic

| | MWRI-ASI SIC (%) | | | SSMI-ASI SIC (%) | | | AMSR-ASI SIC (%) | | |
|---|---|---|---|---|---|---|---|---|---|
| | [15:30) | [30:70) | [70:100] | [15:30) | [30:70) | [70:100] | [15:30) | [30:70) | [70:100] |
| [-100:-80) | 1 | 0 | 0 | 0 | 0 | 0 | 0 | 0 | 0 |
| [-80:-60) | 6 | 0 | 0 | 11 | 0 | 0 | 14 | 1 | 0 |
| [-60:-40) | 12 | 5 | 0 | 15 | 8 | 0 | 14 | 9 | 0 |
| [-40:-20) | 11 | 22 | 2 | 16 | 26 | 3 | 20 | 25 | 1 |
| [-20:0) | 27 | 21 | 46 | 25 | 17 | 40 | 25 | 21 | 32 |
| [0:20) | 43 | 23 | 35 | 33 | 22 | 39 | 27 | 20 | 48 |
| [20:40) | 0 | 20 | 9 | 1 | 19 | 10 | 0 | 17 | 11 |
| [40:60) | 0 | 9 | 5 | 0 | 8 | 6 | 0 | 6 | 5 |
| [60:80) | 0 | 0 | 3 | 0 | 0 | 2 | 0 | 0 | 3 |
| [80:100] | 0 | 0 | 0 | 0 | 0 | 0 | 0 | 0 | 0 |

0  8  16  24  32  40  48  56   Proportion of data pairs (%)

**Figure 7: Proportion of data pairs (number in the grid) of the PM SIC products vs SIC differences between the PM SIC products and ship-based SIC. The PM SIC is divided to three categories of 15–30%, 30–70%, and 70–100% (horizontal axis). The SIC differences are grouped with an interval of 20% (vertical axis).**

17

**Table 5. Biases, MADs. RMSDs, and *Rs* between the PM SIC products and ship-based SIC during the entire overlap periods, as well as the summer and winter months from 2010 to 2019. The 'Count' is the number of data pairs of the individual PM SIC and ship-based SIC.**

| | | Arctic | | | Antarctic | | |
| --- | --- | --- | --- | --- | --- | --- | --- |
| | | MWRI-ASI | SSMI-ASI | AMSR-ASI | MWRI-ASI | SSMI-ASI | AMSR-ASI |
| Overall | Count | 5230 | 5508 | 6169 | 2599 | 2613 | 2979 |
| | bias (%) | 2 | 3 | 6 | 3 | 1 | 4 |
| | MAD (%) | 16 | 15 | 16 | 17 | 18 | 16 |
| | RMSD (%) | 23 | 22 | 23 | 23 | 24 | 23 |
| | *R* | 0.60** | 0.66** | 0.57** | 0.62** | 0.57** | 0.57** |
| Winter | Count | 649 | 655 | 670 | 696 | 794 | 910 |
| | bias (%) | -4 | -4 | -0.2 | 3 | 0.7 | 3 |
| | MAD (%) | 12 | 11 | 7 | 14 | 14 | 13 |
| | RMSD (%) | 19 | 18 | 15 | 19 | 20 | 20 |
| | *R* | 0.44** | 0.53** | 0.42** | 0.67** | 0.64** | 0.58** |
| Summer | Count | 4581 | 4853 | 5499 | 1903 | 1819 | 2069 |
| | bias (%) | 2 | 3 | 7 | 3 | 2 | 5 |
| | MAD (%) | 17 | 16 | 17 | 18 | 20 | 18 |
| | RMSD (%) | 23 | 22 | 24 | 24 | 26 | 25 |
| | *R* | 0.59** | 0.66** | 0.55** | 0.59** | 0.53** | 0.56** |
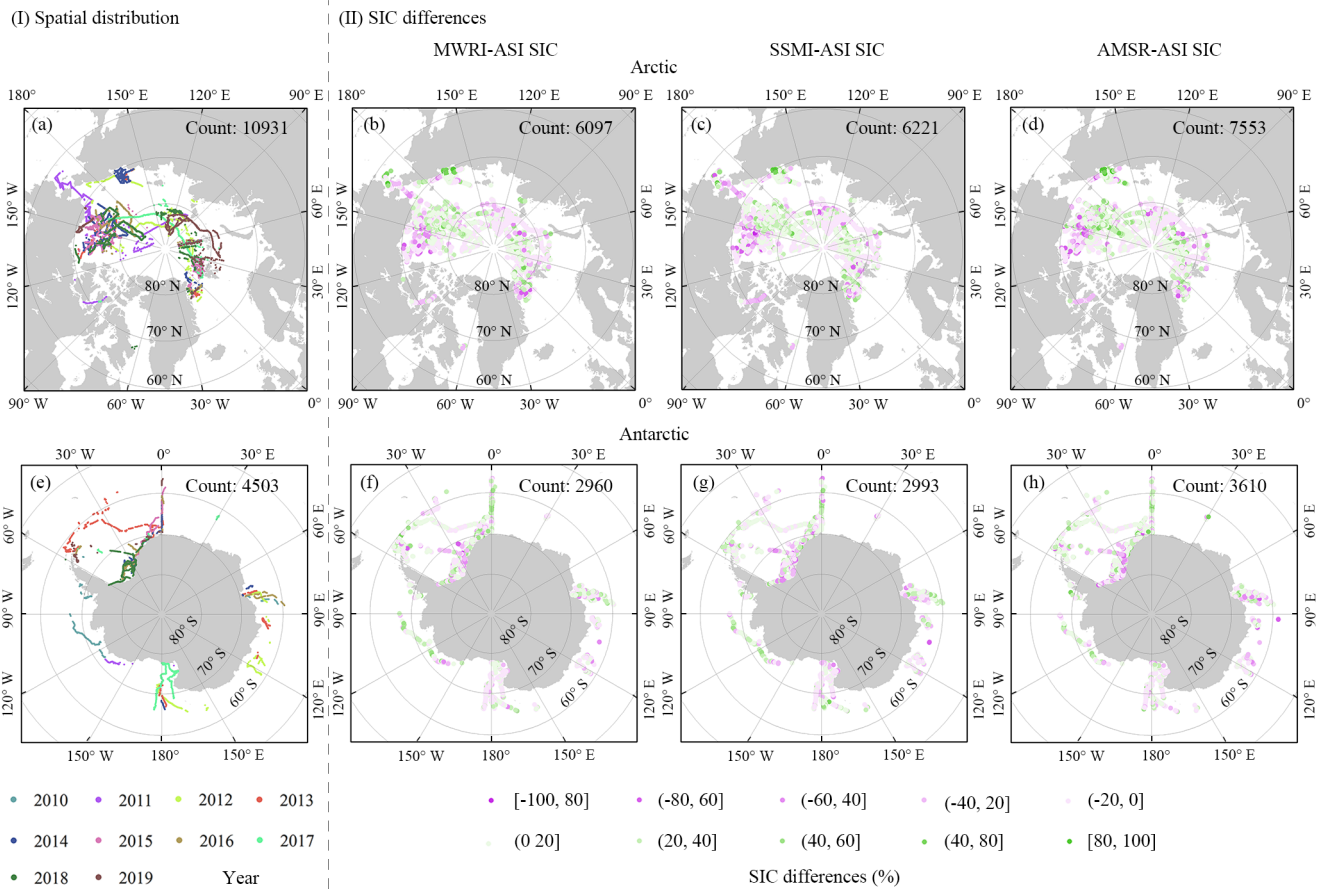
Figure 8: (I). Spatial distributions of the ship-based observational SIC in 2010–2019. (II). SIC differences between the PM SIC products and ship-based observations.

## 4 Discussion

### 4.1 TB differences among the MWRI, SSMI, and AMSR series sensors

At the frequencies used for calculating SIC, i.e., at 89 GHz with V- and H-polarization and differences between them (defined as polarization differences), the MWRI TB is closer to the AMSR TB than the SSMI TB (Table 6). In the PIZ, the MADs of polarization difference at 89 GHz between the MWRI TB and SSMI TB are smaller with values of 1.5 and 1.7 K in the Arctic and Antarctic, respectively, compared to those in the MIZ (4.6 and 4.4 K) and over open water (7.6 and 7.6 K), where the atmospheric influence is more intense. Overall, the polarization difference at 89 GHz of the MWRI sensor is slightly higher than that of the SSMI sensor with a mean positive bias of 0.9 K and slightly lower than that of the AMSR sensor with a mean negative bias of -1.1 K. It illustrates that the re-calibrated MWRI TB is comparable to the SSMI and AMSR TB, which can be well applied to the ASI algorithm.

19

The TB differences between the MWRI and SSMI sensor are smaller than those between MWRI and AMSR sensor at low frequencies used for the weather filters. The overall biases between MWRI TB and SSMI TB are -1.2, -0.7, and 0.1 K at 18.7, 23.8, and 36.5 GHz with V-polarization, respectively. Compared to the AMSR TB, the MWRI TB is lower with mean biases of -5.3, -5.4, and -3.9 K at 18.7, 23.8, and 36.5 GHz with V-polarization, respectively. In general, the low frequencies of MWRI sensor can filter the weather effects, which is similar to those of the SSMI and AMSR sensors.

**Table 6. MADs between the MWRI TB and other two TBs in the PIZ, MIZ, and open water from 2010 to 2019. The first and second numbers in each cell present the MADs between the MWRI TB and SSMI TB, and those between the MWRI TB and AMSR TB.**

|  | Arctic (K) | | | Antarctic (K) | | |
|---|---|---|---|---|---|---|
|  | PIZ | MIZ | Open water | PIZ | MIZ | Open water |
| 18 V | 1.7 / 4.0 | 4.8 / 7.2 | 7.4 / 11.4 | 2.4 / 4.5 | 3.6 / 6.6 | 4.8 / 9.5 |
| 23 V | 2.0 / 4.1 | 4.5 / 6.2 | 7.0 / 11.4 | 2.3 / 4.7 | 3.5 / 6.5 | 4.3 / 9.1 |
| 36 V | 2.5 / 2.8 | 4.1 / 4.7 | 6.3 / 9.2 | 2.5 / 3.0 | 3.4 / 4.9 | 4.2 / 6.3 |
| 89 V | 3.9 / 3.5 | 4.6 / 3.4 | 13.8 / 7.1 | 4.1 / 3.3 | 4.2 / 3.6 | 8.1 / 4.0 |
| 89 H | 4.3 / 3.8 | 7.4 / 5.5 | 18.1 / 10.7 | 4.9 / 3.8 | 7.1 / 5.4 | 14.1 / 8.3 |
| 89 V – 89 H | 1.5 / 1.3 | 4.6 / 4.1 | 7.6 / 6.0 | 1.7 / 1.5 | 4.4 / 3.8 | 7.6 / 5.7 |

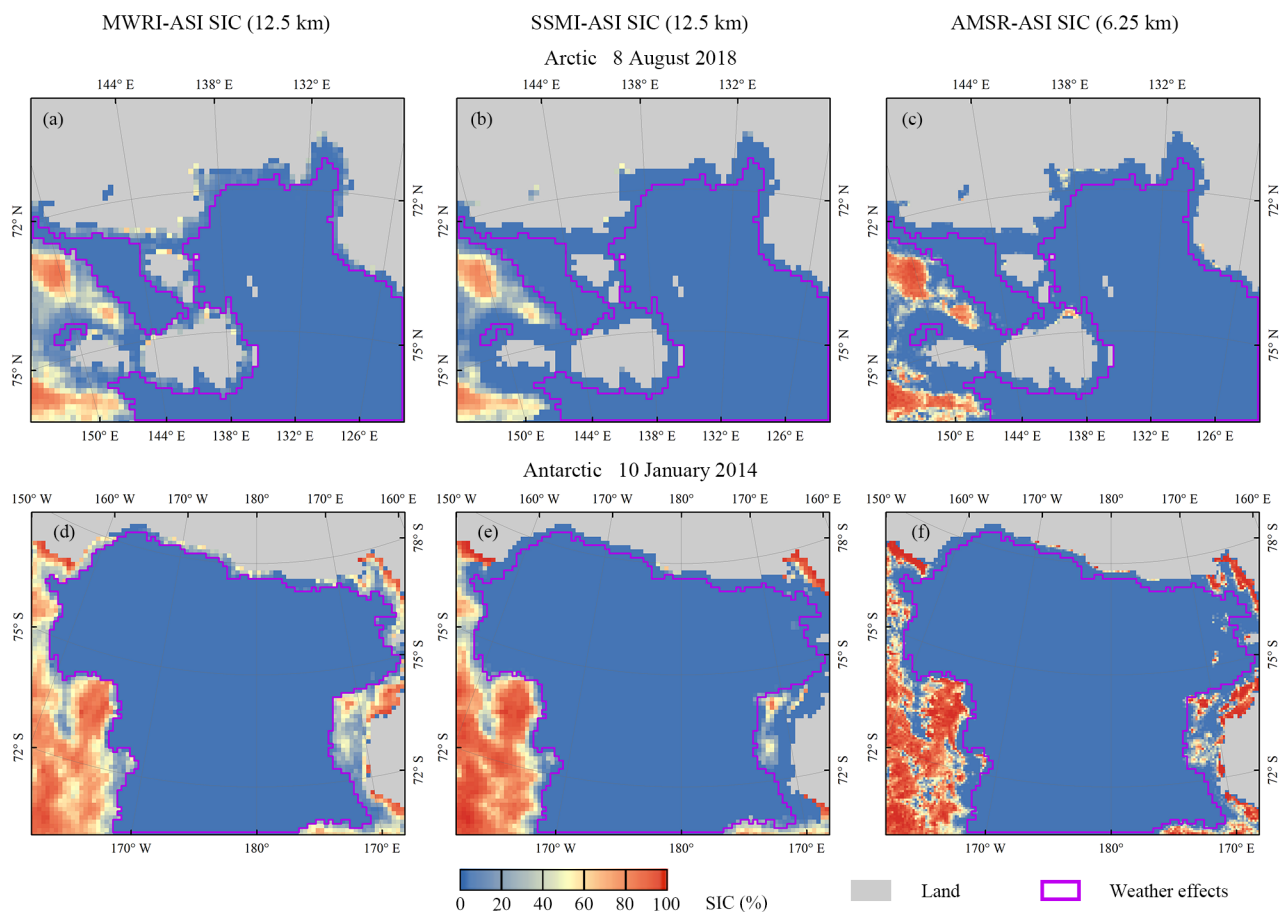## 4.2 Improvements and limitations of the MWRI-ASI v2 SIC

Compared to the previous version of MWRI-ASI SIC generated by Zhao et al. (2022) (MWRI-ASI v1 SIC), the MWRI-ASI SIC generated by this study (MWRI-ASI v2 SIC) is lower by -3% in the Arctic in 2018, especially in the MIZ and in summer. The MWRI-ASI v1 SIC has small differences against AMSR-ASI SIC, but the time series of AMSR-ASI is shorter than the SSMI-ASI SIC. To obtain longer-term SIC products, this study modified the previous algorithm and adopted the SSMI-ASI SIC as referential SIC to update and extend the MWRI-ASI SIC. The MWRI TB applied for the MWRI-ASI v1 SIC were bias-corrected using the AMSR2 TB by a linear aggression during only one-year overlap period of 2018. As a result, the systematic deviations between the MWRI-ASI v1 SIC and AMSR-ASI SIC increased in 2019 compared to those in 2018, especially in summer (Chen et al., 2021). To obtain a more consistent SIC product, the re-calibrated MWRI TB were adopted as input source TB, because the differences among the re-calibrated MWRI TB from different satellites were low with mean of 2.8 and 1.0 K in the Arctic and Antarctic, respectively. From 2018 to 2019, when only the FY-3D MWRI TB were used, the differences in systematic deviations between the MWRI-ASI v2 SIC and AMSR-ASI SIC were 0.6% in summer, which were relatively small compared to those (1%) between the MWRI-ASI v1 SIC and AMSR-ASI SIC. It indicates that the consistency of the MWRI-ASI v2 SIC is improved compared with the MWRI-ASI v1 SIC.

However, the MWRI-ASI SIC v2 is still limited in terms of the land spillover and weather effects. Due to the differences in the size of the view field of different TB frequencies and the differences in observational TB of open water and land, the spurious sea ice would emerge in the PM observations along the coasts (Lavergne et al., 2019; Kern et al., 2019). Although some methods have been proposed to solve the land spillover by expanding the land mask (Maslanik et al., 1996), subtracting

the summer minimum SIC from original images (Cavalieri et al., 1996), and estimating the fraction of land emissivity in the

425 TB (Maaß and Kaleschke, 2010), the SIC differences are still higher in the near-coast regions than in the regions far away from the coast. The SIC MADs between the MWRI-ASI and SSMI-ASI within 50 km away from the coast are larger with values of 6% in the Arctic and of 7% in the Antarctic, compared to those (4% and 5%) beyond 50 km away from the coast. The MADs within 50 km away from the coast between MWRI-ASI SIC and AMSR-ASI SIC are 8% in the Arctic and 9% in the Antarctic, which are higher than those (5% and 6%) beyond 50 km away from the coast. Compared to the SSMI-ASI and

430 AMSR-ASI, the MWRI-ASI reveals more ice along the coasts and around the islands, such as around 72° N from 138° E to 144° E in the Arctic and around 78° S from 160° W to 170° E in the Antarctic (Fig. 9). The ice along the coast extends about two grids (25 km) from the coastline, leading to the overestimation of the MWRI-ASI SIE in summer compared to the SSMI-ASI SIE. Due to larger uncertainties of our MWRI-ASI SIC in the near-coast region, it is recommended that the grids extended outward from the coast by 50 km can be removed when using it.

435 To analyze the influence of temporal filter on land spillover, we acquired the single-day SSMI-ASI SIC product (Single-day SSMI-ASI) from the French Research Institute for Exploitation of the Sea via the Centre d'Exploitation et de Recherche SATellitaire (Ifremer/CERSAT) (Girard-Ardhuin et al., 2008). The SSMI-ASI SIC produced by Hamburg Uni were filtered by a five-day median filter (Five-day SSMI-ASI). In the region within 50 km away from the coast, the SIC MADs between MWRI-ASI and Single-day SSMI-ASI are 6% in both the Arctic and the Antarctic, which are slightly smaller than those

440 between MWRI-ASI and Five-day SSMI-ASI by 0.4%. It indicates that the SIC uncertainties in the near-coast regions would be slightly increased after temporal filter.

The spurious sea ice over open water arises from the atmospheric effect, i.e., water vapor, cloud liquid water, surface winds, and precipitation (Kern, 2004). Although the methods to remove the spurious ice have been applied, some spurious floes remain and some small real floes are ignored in the MIZ. The MWRI-ASI weather filters can remove most of the spurious ice

445 (Fig, 9). However, after applying the weather filters, more ice floes have been identified by the MWRI-ASI in the MIZ compared to the SSMI-ASI and AMSR-ASI. It is still difficult to determine whether this residual ice is erroneous ice caused by weather effects or the real discrete small ice floes. Thus, in the future work, we will attempt to identify and remove the spurious ice caused by land spillover and weather effects, by combining the optical or synthetic aperture radar images with higher resolutions, to further improve our MWRI-ASI SIC product.

MWRI-ASI SIC (12.5 km)    SSMI-ASI SIC (12.5 km)    AMSR-ASI SIC (6.25 km)

Arctic   8 August 2018

Antarctic   10 January 2014

0   20   40   60   80   100   SIC (%)          Land          Weather effects

**Figure 9: SIC distributions of the MWRI-ASI, SSMI-ASI, and AMSR-ASI in the coastal regions. Also shown are the weather-affected grids removed by the MWRI-ASI weather filters.**

## 4.3 Comparisons to prior studies on SIC products in the polar regions

The biases between our MWRI-ASI SIE and Sea Ice Index SIE from 2015 to 2017 are $-0.3\times10^6$ km$^2$ in the Arctic and $0.2\times10^6$ km$^2$ in the Antarctic, respectively, which are within the range of SIE biases in the same period shown in Meier and Stewart (2019). Seasonally, in the bipolar regions, our MWRI-ASI SIE has larger absolute deviations against the Sea Ice Index SIE in winter than in summer. The reduction of absolute deviation of Arctic SIE in summer is because our MWRI-ASI SIE has been involved more sea ice along the coastline and at the ice edge in summer than in winter. In the Antarctic, our MWRI-ASI SIE is about two grids (25 km) farther south than the Sea Ice Index SIE, and the absolute deviation increases in winter because the SIE is larger in winter than in summer. The seasonal variation pattern of biases between our MWRI-ASI SIE and Sea Ice Index SIE is similar to those between the AMSR-BST SIE and Sea Ice Index SIE in the Arctic (Meier and Stewart, 2019).

Beitsch et al. (2015) revealed that the accuracies of the AMSR-E ASI SIC and SSMI-ASI SIC are consistent, with overall RMSDs of about 13% compared to the ASPeCt observations from 2002 to 2010. Our study also indicates that the accuracy of

22

the MWRI-ASI SIC is comparable to those of the SSMI-ASI SIC and AMSR-ASI SIC, with overall RMSDs of about 23%

465    compared to the ship-based observations from 2010 to 2019. The accuracy of our MWRI-ASI SIC is lower in summer than in winter, which is consistent with those of the AMSR-E ASI SIC and SSMI-ASI SIC (Beitsch et al., 2015). This study and the results given by Spreen et al., (2008) both presented that the SIC differences between PM-based and ship-based observations are larger in the low-SIC region than those in the high-SIC region. The large SIC differences can be explained by the different spatial and temporal scales between PM SICs and ship-based SICs (Beitsch et al., 2015; Kern et al., 2019). Ship-based SICs

470    are obtained on an elliptically shaped area of 1 km on each side of the ship, while the footprint sizes of PM frequencies were considerably larger than 1 km, which are several kilometers to tens of kilometers. In contrast to ship-based SIC gained by observers at a specific time, the PM SICs are the daily averages combined with swath SICs from different time in one calendar day. The ship-based SIC may not be fully representative of the entire grid of PM SIC and the observation results may also be affected by visibility and light around the ship.

475    **5 Data availability**

The SIC product is derived from the FY-3 MWRI sensors, which can be downloaded from the data repositories PANGAEA at https://doi.pangaea.de/10.1594/PANGAEA.945188 (Chen et al., 2022). This dataset is available from 12 November 2010 to 31 December 2019 with temporary data gaps of 23 days in the Arctic and 82 days in the Antarctic. The SIC files are named "FY_MWRI_SIC_DAILY_YYYYMMDD_Region.tif", with "YYYYMMDD" denoting the date and "Region" representing

480    the Arctic or Antarctic. This SIC dataset is archived in TIFF format and can be read using Python, ENVI/IDL, and MATLAB software. The values '0-100' are the percentage of SIC, flag of '-1' is the land and of '-2' is the Pole Hole, and 'NoData' is the missing data. Additionally, the biases between this SIC dataset and other two ASI SIC products, i.e., SSMI-ASI and AMSR-ASI, are provided.

   **6 Conclusion**

485    This study generates a new SIC product in the polar regions from November 2010 to December 2019, which is derived from the recent re-calibrated TB data of the MWRI sensors onboard the FY-3B, FY-3C, and FY-3D satellites using the modified dynamic tie points ASI algorithm. Generally, the MWRI-ASI SIC or SIE can reasonably identify the seasonal and long-term changes in sea ice, as well as the extreme cases of annual maximum/minimum SIE for both the Arctic and Antarctic.

To test the ability of the MWRI-ASI as an independent PM SIC dataset, the MWRI-ASI SIC is compared to the existing ASI

490    SIC products of SSMI-ASI and AMSR-ASI, and the MWRI-ASI SIE is compared to the existing SIE products of SSMI-BST, SSMI-NT, OSI-SAF, and Sea Ice Index. The accuracy of the MWRI-ASI SIC is also validated using the ship-based observed SIC.

Both the daily SIC and SIE derived from the MWRI-ASI closely agree with those derived from the SSMI-ASI, with overall SIC biases of -1% and 0.5%, and with overall SIE biases of $0.1\times10^6$ km$^2$ and $-0.02\times10^6$ km$^2$ in the Arctic and Antarctic, respectively. The ability of the MWRI-ASI to identify the MIZ mostly coincides with that of the SSMI-ASI. Therefore, the MWRI-ASI SIC is closer to the SSMI-ASI SIC compared to AMSR-ASI SIC. The MWRI-ASI SIC has larger uncertainties in the region with low or medium SIC than in the region with high SIC. Shallower snow depth over sea ice cause larger uncertainties of SIC, especially during the summer. The sensitivity of MWRI-ASI SIC to sea ice melting surface is higher than the SSMI-ASI, which suggests the MWRI-ASI SIC product may have better ability to identify the melting surface.

The MWRI-ASI SIE has smaller differences against the Sea Ice Index SIE in the Arctic and against the OSI-SAF SIE in the Antarctic compared to other products. Based on the comparison with the ship-based observations, the accuracy of the MWRI-ASI SIC is comparable to those of the SSMI-ASI SIC and AMSR-ASI SIC. It suggests the MWRI-ASI SIC product can be independently used for monitoring changes in sea ice and serve as reliable data to evaluate the next-generation sensors. Following this study, we will attempt to identify and remove the spurious sea ice caused by land spillover and weather effects more accurately by using satellite-based observations with higher resolutions to further improve the MWRI-ASI SIC. In addition, based on the re-calibrated TB data of the MWRI sensors, we can produce other geophysical variables for the sea ice in the polar regions, e.g., lead fraction, onsets of ice surface melt or freeze, and other morphological characteristics.

**Author Contributions.**

YC performed the experiments and wrote the manuscript. XP, RL, and XZ provided the conception of the study and suggestions on manuscript. SW and PZ provided valuable instructions on data and methods. YL, PF, and QJ advised on the model code. All authors contributed to the improvement of the manuscript.

**Competing interests.**

The authors declare that they have no conflict of interest.

Ocean and Sea Ice Satellite Application Facility (OSI-SAF) provided the OSI-SAF SIE datasets. The U.S. Geological Survey (USGS), NASA Goddard Earth Science Projects provided the Arctic sea ice surface melt/freeze onset data. The French Research Institute for Exploitation of the Sea provided the Single-day SSMI-ASI SIC product. We also want to acknowledge the contributors of the ship-based observed SIC in the IceWatch and PANGAEA databases, as well as during the CHINARE cruises.

# References

Beitsch, A., Kern, S., and Kaleschke, L.: Comparison of SSM/I and AMSR-E sea ice concentrations with ASPeCt ship observations around Antarctica, IEEE Trans. Geosci. Remote Sens., 53, 1985–1996, https://doi.org/10.1109/TGRS.2014.2351497, 2015.

Cavalieri, D. J., St Germain, K. M., and Swift, C. T.: Reduction of weather effects in the calculation of sea-ice concentration with the DMSP SSM/I, J. Glaciol., 41, 455–464, https://doi.org/10.1017/S0022143000034791, 1995.

Cavalieri, D. J., Parkinson, C. L., Gloersen, P., and Zwally, H. J.: Sea Ice Concentrations from Nimbus-7 SMMR and DMSP SSM/I-SSMIS Passive Microwave Data, Version 1.User Guide, Natl. Snow Ice Data Center, Boulder, Color. USA, 0–29, 1996.

Cavalieri, D. J., Markus, T., and Comiso., J. C.: AMSR-E/Aqua Daily L3 12.5 km Brightness Temperature, Sea Ice Concentration, & Snow Depth Polar Grids, Version 3, Boulder, Color. USA. NASA Natl. Snow Ice Data Cent. Distrib. Act. Arch. Center., https://doi.org/10.5067/AMSR-E/AE_SI12.003, 2014.

Chen, Y., Zhao, X., Pang, X., and Ji, Q.: Daily sea ice concentration product based on brightness temperature data of FY-3D MWRI in the Arctic, Big Earth Data, 00, 1–15, https://doi.org/10.1080/20964471.2020.1865623, 2021.

Chen, Y., Pang, X., Lei, R., and Zhao, X.: Sea ice concentration derived from temperature brightness data of the Microwave Radiation Imager sensors onboard the Chinese FengYun-3 satellites in the polar regions from 2010 to 2019, https://doi.org/https://doi.pangaea.de/10.1594/PANGAEA.945188, 2022.

Comiso, J. C., Cavalieri, D. J., and Markus, T.: Sea ice concentration, ice temperature, and snow depth using AMSR-E data, IEEE Trans. Geosci. Remote Sens., 41, 243–252, https://doi.org/10.1109/TGRS.2002.808317, 2003.

Comiso, J. C., Meier, W. N., and Gersten, R.: Variability and trends in the Arctic Sea ice cover: Results from different techniques, J. Geophys. Res. Ocean., 122, 6883–6900, https://doi.org/10.1002/2017JC012768, 2017.

25

550     Eisenman, I., Meier, W. N., and Norris, J. R.: A spurious jump in the satellite record: Has Antarctic sea ice expansion been overestimated?, 8, 1289–1296, https://doi.org/10.5194/tc-8-1289-2014, 2014.

Fetterer, F., Knowles, K., Meier, W. N., Savoie, M. H., and Windnagel, A. K.: updated daily. Sea Ice Index, Version 3. [Monthly Sea Ice Extent], Boulder, Color. USA. NSIDC Natl. Snow Ice Data Center., https://doi.org/10.7265/N5K072F8, 2017.

555     Gerland, S., Barber, D., Meier, W., Mundy, C. J., Holland, M., Kern, S., Li, Z., Michel, C., Perovich, D. K., and Tamura, T.: Essential gaps and uncertainties in the understanding of the roles and functions of Arctic sea ice, Environ. Res. Lett., 14, https://doi.org/10.1088/1748-9326/ab09b3, 2019.

Girard-Ardhuin, F., Ezraty, R., and Croizé-Fillon, D.: Arctic and Antarctic sea ice concentration and sea ice drift satellite products at Ifremer/CERSAT, Q. Newsletter, 34, 31–39, 2008.

560     Gloersen, P. and Cavalieri, D. J.: Reduction of weather effects in the calculation of sea ice concentration from microwave radiances, J. Geophys. Res., 91, 3913, https://doi.org/10.1029/jc091ic03p03913, 1986.

Heil, P., Fowler, C. W., and Lake, S. E.: Antarctic sea-ice velocity as derived from SSM/I imagery, Ann. Glaciol., 44, 361–366, https://doi.org/10.3189/172756406781811682, 2006.

Hutchings, J., Delamere, J., and Heil, P.: The Ice Watch Manual, 2019.

565     Ivanova, N., Pedersen, L. T., Tonboe, R. T., Kern, S., Heygster, G., Lavergne, T., Sørensen, A., Saldo, R., Dybkjær, G., Brucker, L., and Shokr, M.: Inter-comparison and evaluation of sea ice algorithms: Towards further identification of challenges and optimal approach using passive microwave observations, 9, 1797–1817, https://doi.org/10.5194/tc-9-1797-2015, 2015.

Jiménez, C., Tenerelli, J., Prigent, C., Kilic, L., Lavergne, T., Skarpalezos, S., Høyer, J. L., Reul, N., and Donlon, C.: Ocean and Sea Ice Retrievals From an End-To-End Simulation of the Copernicus Imaging Microwave Radiometer (CIMR) 1.4–
570     36.5 GHz Measurements, J. Geophys. Res. Ocean., 126, 1–23, https://doi.org/10.1029/2021JC017610, 2021.

Kaleschke, L., Lüpkes, C., Vihma, T., Haarpaintner, J., Bochert, A., Hartmann, J., and Heygster, G.: SSM/I sea ice remote sensing for mesoscale ocean-atmosphere interaction analysis, Can. J. Remote Sens., 27, 526–537, https://doi.org/10.1080/07038992.2001.10854892, 2001.

Kern, S.: A new method for medium-resolution sea ice analysis using weather-influence corrected Special Sensor
575     Microwave/Imager 85 GHz data, Int. J. Remote Sens., 25, 4555–4582, https://doi.org/10.1080/01431160410001698898, 2004.

Kern, S.: ESA-CCI_Phase2_Standardized_Manual_Visual_Ship-Based_SeaIceObservations_v02, World Data Cent. Clim. DKRZ, https://doi.org/10.26050/WDCC/ESACCIPSMVSBSIOV2, 2019.

Kern, S., Rösel, A., Toudal Pedersen, L., Ivanova, N., Saldo, R., and Tage Tonboe, R.: The impact of melt ponds on summertime microwave brightness temperatures and sea-ice concentrations, 10, 2217–2239, https://doi.org/10.5194/tc-10-
580     2217-2016, 2016.

Kern, S., Lavergne, T., Notz, D., Toudal Pedersen, L., Tage Tonboe, R., Saldo, R., and Macdonald Sørensen, A.: Satellite passive microwave sea-ice concentration data set intercomparison: Closed ice and ship-based observations, 13, 3261–3307, https://doi.org/10.5194/tc-13-3261-2019, 2019.

Kern, S., Kaleschke, L., Girard-Ardhuin, F., Spreen, G., and Beitsch, A.: Global daily gridded 5-day median-filtered, gap-filled ASI Algorithm SSMI-SSMIS sea ice concentration data, Integr. Clim. Date Cent. (ICDC), CEN, Univ. Hamburg, Ger., https://www.cen.uni-hamburg.de/en/icdc/data/cryosphere/seaiceconcentration-asi-ssmi.html, 2020.

Lavergne, T., Macdonald Sørensen, A., Kern, S., Tonboe, R., Notz, D., Aaboe, S., Bell, L., Dybkjær, G., Eastwood, S., Gabarro, C., Heygster, G., Anne Killie, M., Brandt Kreiner, M., Lavelle, J., Saldo, R., Sandven, S., and Pedersen, L. T.: Version 2 of the EUMETSAT OSI SAF and ESA CCI sea-ice concentration climate data records, 13, 49–78, https://doi.org/10.5194/tc-13-49-2019, 2019.

Lavergne, T., Aaboe, S., Neuville, A., Macdonald Sørensen, A., and Eastwood, S.: Product User Manual for the Sea Ice Index, version 2.1, 1–18, 2020.

Lavergne, T., Kern, S., Aaboe, S., Derby, L., Dybkjaer, G., Garric, G., Heil, P., Hendricks, S., Holfort, J., Howell, S., Key, J., Lieser, J. L., Maksym, T., Maslowski, W., Meier, W., Munoz-Sabater, J., Nicolas, J., Özsoy, B., Rabe, B., Rack, W., Raphael, M., de Rosnay, P., Smolyanitsky, V., Tietsche, S., Ukita, J., Vichi, M., Wagner, P., Willmes, S., and Zhao, X.: A New Structure for the Sea Ice Essential Climate Variables of the Global Climate Observing System, Bull. Am. Meteorol. Soc., 1–41, https://doi.org/10.1175/bams-d-21-0227.1, 2022.

Lei, R., Tian-Kunze, X., Li, B., Heil, P., Wang, J., Zeng, J., and Tian, Z.: Characterization of summer Arctic sea ice morphology in the 135°-175°W sector using multi-scale methods, Cold Reg. Sci. Technol., 133, 108–120, https://doi.org/10.1016/j.coldregions.2016.10.009, 2017.

Li, N., Lei, R., Heil, P., Cheng, B., Ding, M., Tian, Z., and Li, B.: Seasonal and interannual variability of the landfast ice mass balance between 2009 and 2018 in Prydz Bay , East Antarctica, Cryosph., 917–937, https://doi.org/https://doi.org/10.5194/tc-17-917-2023, 2023.

Maaß, N. and Kaleschke, L.: Improving passive microwave sea ice concentration algorithms for coastal areas: Applications to the Baltic Sea, Tellus, Ser. A Dyn. Meteorol. Oceanogr., 62, 393–410, https://doi.org/10.1111/j.1600-0870.2010.00452.x, 2010.

Markus, T., Stroeve, J. C., and Miller, J.: Recent changes in Arctic sea ice melt onset, freezeup, and melt season length, J. Geophys. Res. Ocean., 114, 1–14, https://doi.org/10.1029/2009JC005436, 2009.

Maslanik, J. A., Serreze, M. C., and Barry, R. G.: Recent decreases in Arctic summer ice cover and linkages to atmospheric circulation anomalies, Geophys. Res. Lett., 23, 1677–1680, https://doi.org/10.1029/96GL01426, 1996.

Meier, W. N.: Satellite passive microwave observations of sea ice, 3rd ed., Elsevier Inc., 402–414 pp., https://doi.org/10.1016/B978-0-12-409548-9.11461-7, 2019.

Meier, W. N. and Ivanoff, A.: Intercalibration of AMSR2 NASA Team 2 Algorithm Sea Ice Concentrations with AMSR-E Slow Rotation Data, IEEE J. Sel. Top. Appl. Earth Obs. Remote Sens., 10, 3923–3933, https://doi.org/10.1109/JSTARS.2017.2719624, 2017.

Meier, W. N. and Stewart, J. S.: Assessing uncertainties in sea ice extent climate indicators, Environ. Res. Lett., 14, https://doi.org/10.1088/1748-9326/aaf52c, 2019.

Meier, W. N., Markus, T., and Comiso, J. C.: AMSR-E/AMSR2 Unified L3 Daily 12.5 km Brightness Temperatures, Sea Ice Concentration, Motion & Snow Depth Polar Grids, Version 1, Boulder, Color. USA. NASA Natl. Snow Ice Data Cent. Distrib.

620 Act. Arch. Center., https://doi.org/10.5067/RA1MIJOYPK3P, 2018.

Meier, W. N., Stewart, J. S., Wilcox, H., Scott, D. J., and Hardman, M. A.: DMSP SSM/I-SSMIS Daily Polar Gridded Brightness Temperatures, Version 6, Boulder, Color. USA. NASA Natl. Snow Ice Data Cent. Distrib. Act. Arch. Center., https://doi.org/10.5067/MXJL42WSXTS1, 2021.

Melsheimer, C. and Spreen, G.: AMSR-E/AMSR2 ASI sea ice concentration data,Arctic, Antarctica version 5.4 (NetCDF),

625 https://doi.org/10.1594/PANGAEA.898400, 2020.

Newell, D., Draper, D., Remund, Q., Woods, B., Mays, C., Bensler, B., Miller, D., and Eastman, K.: Weather Satellite Follow-On–Microwave (WSF-M) design and predicted performance, Ball Aerospace, Boulder, Color. USA, 2020.

Parkinson, C. L. and DiGirolamo, N. E.: Sea ice extents continue to set new records: Arctic, Antarctic, and global results, Remote Sens. Environ., 267, 112753, https://doi.org/10.1016/j.rse.2021.112753, 2021.

630 Spreen, G., Kaleschke, L., and Heygster, G.: Sea ice remote sensing using AMSR-E 89-GHz channels, J. Geophys. Res. Ocean., 113, 1–14, https://doi.org/10.1029/2005JC003384, 2008.

Stroeve, J. and Meier, W. N.: Sea Ice Trends and Climatologies from SMMR and SSM/I-SSMIS, Version 3. Monthly total Sea Ice Extent Data, Boulder, Color. USA. NASA Natl. Snow Ice Data Cent. Distrib. Act. Arch. Center., https://doi.org/10.5067/IJ0T7HFHB9Y6, 2018.

635 Svendsen, E., Matzler, C., and Grenfell, T. C.: A model for retrieving total sea ice concentration from a spaceborne dual-polarized passive microwave instrument operating near 90 GHz, Int. J. Remote Sens., 8, 1479–1487, https://doi.org/10.1080/01431168708954790, 1987.

Trewin, B., Cazenave, A., Howell, S., Huss, M., Isensee, K., Palmer, M. D., Tarasova, O., and Vermeulen, A.: Headline indicators for global climate monitoring, Bull. Am. Meteorol. Soc., 102, E20–E37, https://doi.org/10.1175/BAMS-D-19-

640 0196.1, 2021.

Worby, A. P. and Allison, I.: A ship-based technique for observing Antarctic sea ice. Part I: Observational techniques and results, 1999.

Wu, S. and Liu, J.: Comparison of Arctic sea ice concentration datasets, Acta Ocean. Sin, 40, 64–72, https://doi.org/10.3969/j.issn.0253-4193.2018.11.007, 2018.

645 Xian, D., Zhang, P., Gao, L., Sun, R., Zhang, H., and Jia, X.: Fengyun Meteorological Satellite Products for Earth System Science Applications, Adv. Atmos. Sci., 38, 1267–1284, https://doi.org/10.1007/s00376-021-0425-3, 2021.

Xie, H., Lei, R., Ke, C., Wang, H., Li, Z., Zhao, J., and Ackley, S. F.: Summer sea ice characteristics and morphology in the Pacific Arctic sector as observed during the CHINARE 2010 cruise, 7, 1057–1072, https://doi.org/10.5194/tc-7-1057-2013, 2013.

650 Zhang, P., Chen, L., Xian, D., Zhe, X., Peng, Z., Lin, C., and Di, X.: Recent progress of Fengyun meteorology satellites, Chin. J. Sp. Sci, 38, 788–796, https://doi.org/10.11728/cjss2018.05.788, 2018.

Zhang, P., Lu, Q., Hu, X., Gu, S., Yang, L., Min, M., Chen, L., Xu, N., Sun, L., Bai, W., Ma, G., and Xian, D.: Latest Progress of the Chinese Meteorological Satellite Program and Core Data Processing Technologies, Adv. Atmos. Sci., 36, 1027–1045, https://doi.org/10.1007/s00376-019-8215-x, 2019.

655 Zhao, X., Chen, Y., Kern, S., Qu, M., Ji, Q., Fan, P., and Liu, Y.: Sea Ice Concentration Derived from FY-3D MWRI and Its Accuracy Assessment, IEEE Trans. Geosci. Remote Sens., 60, https://doi.org/10.1109/TGRS.2021.3063272, 2022.